Utrecht University

Joris H.E. de Rooij
427414

Master's Thesis Earth Surface and Water

Start: 1-2-2021
End: 10-12-2021

Supervisors:
Prof. Dr. Steven de Jong, Prof. Dr. Ad de Roo, and Dr. Michelle van Vliet

Estimating chlorophyll-a concentrations in rivers through analysis of hyperspectral PRISMA imagery

Abstract

It is important to monitor the water quality of rivers, as people are dependent on this source of fresh water, and all other services rivers provide. Chlorophyll-a (chl-a) concentration is an important indicator for a proper quality of water and eutrophication. Hyperspectral satellite imagery can be used to estimate chl-a concentration in surface water, but methods for this have mostly been applied to large water bodies, like lakes, estuaries, and oceans. The aim of this research was to investigate how medium spatial resolution, hyperspectral PRISMA imagery can be used for estimating and monitoring water quality of rivers and at what accuracy. For this, two existing chl-a concentration algorithms, a band-ratio algorithm (Gurlin et al., 2011) and a normal difference chlorophyll index (NDCI) algorithm (Mishra & Mishra, 2012), both using PRISMA bands 34 (665nm) and 38 (709nm), were used. These algorithms were validated using a local chl-a concentration and reflectance dataset (n=11) of the Danube-Sava confluence. These algorithms were also recalibrated and validated using this same dataset to investigate if the results improve. The original Mishra and Mishra NDCI algorithm had the overall best performance, with a NMAE of 0.07 and a NRMSE of 0.09. It was possible to map spatial patterns of chl-a in rivers with qualitative concentration estimates and to refine that into quantitative estimates with a certain uncertainty range. The performance of both algorithms did not improve after recalibration. Large-scale sources of chl-a in rivers, like larger tributaries, could be deduced from the chl-a distribution maps, showing that the Danube has a higher chl-concentration than the Sava before the confluence. The (limited) mixing of water at the confluence and the distribution of chl-a after the confluence could be observed and interpreted. Small scale sources of chl-a, like wastewater outlets, could not be deduced in this research as the spatial resolution of the chl-a distribution maps was still too high compared the small and localized chl-a influx of these sources. With further validation of the Mishra and Mishra NDCI algorithm using a more extensive dataset, these methods could be developed into an automated monitoring system, as medium resolution hyperspectral imagery is suitable for estimating and monitoring the water quality of rivers.

Table of content

Abbreviations and symbols

ANN	Artificial neural networks
ASI	Agenzia Spaziale Italiana
Chl-a	Chlorophyll-a
GCP	Ground control points
λ	Wavelength
MAE	Mean average error
NDCI	Normalized difference chlorophyll index
NDVI	Normalized difference vegetation index
NIR	Near-infrared
NMAE	Normalized mean absolute error
NRMSE	Normalized root mean square error
R	Reflectance
$\bar{R}$	Average reflectance
R^2	Coefficient of determination
RMSE	Root mean square error
SD	Standard deviation
SWIR	Shortwave infrared
TOA	Top of the atmosphere
TSS	Total suspended solids
VNIR	Visible and near-infrared
WDF	Water directive frame
$\propto$	Is proportional to

1. Introduction and background

1.1. The importance of river water quality

Human population depends on fresh and clean water, and thus people tend to concentrate around fresh surface water. 87.5% of the world population lives in the vicinity of a river, ranging from a small stream to the largest rivers on Earth (Kummu et al., 2011). Rivers provide humans with provisioning, spiritual, and regulating and maintaining services (Gilvaer et al., 2016). The provisioning services of rivers are most familiar, as they directly sustain and benefit our society and give the river its economic value. River water is used for drinking water production, irrigation, and industrial processes. Flooding covers the banks of rivers with fertile sediments for agriculture. Rivers maintain an ecosystem from which food like fish and shellfish could be harvested. Rivers are a natural highway for transport of people and bulk goods, and even a sewer that allows waste(water) to be discharged and taken out of sight. The spiritual service gives the rivers a high intrinsic value, as well as an economic value. In many societies, rivers play an important religious role. Recreation also falls under spiritual services, and it is an important one. The river allows for the practice of water sports and provides beautiful scenery, but also its surrounding ecosystem allows for many options for recreation. While the use of these provisioning and spiritual services often depends on a good water quality, many of the rivers uses affect the water quality in a negative way by changing the natural current of rivers and decreasing the water quality. The decrease of river water quality is not only the result of the direct use of the rivers services, as pollutants originating from further away can also be introduced to the river through groundwater. Pollution of rivers affect people's health. Globally, more people die of unsafe water than from any form of violence (including war) combined (UNDESA, 2014). A poor river water quality also affects the health and stability of the ecosystem.

The regulating and maintaining services can be quickly overlooked and not always fully known to the public, but they play a vital role in the stability of both society and ecosystems. These important services include maintaining ecosystems, flood protection, and local climate control. The health and stability of an ecosystem surrounding a river depends on this river and its water quality. Rivers play an important role in flood protection, as rainwater is channelled off and regular small-scale flooding and sediment deposit elevates the land, preventing subsidence and larger floods. Evaporation of waterbodies such as rivers can cool surrounding temperature and increase humidity. A local river ecosystem is a finely balanced system, where small disruptions can have major consequences. These effects can be felt locally, but also further downstream. A decline of the river water quality can limit some of the river's ecological services.

The quality of river water is determined by various properties and constituents. Generally, water quality parameters can be divided into three broad categories, namely physical, chemical, and biological (Sutadian et al., 2016; Swamee & Tyagi, 2007). Common physical water quality parameters include temperature (°C), Total Suspended Matter (TSS) (mg/L), and turbidity (NTU). Examples of chemical water quality parameters include pH(-), dissolved oxygen (mg/L), and biological or chemical oxygen demand (mg/L). Finally, biological water quality parameters include chlorophyll-a (chl-a) concentration and (µg/L) Coloured Dissolved Organic Matter (CDOM) (mg/L). The focus of this research is chl-a, a photosynthetic pigment that can be found in leaves of plants, but also in aquatic algae. This parameter was chosen because not much research on estimating chl-a concentration in rivers through remote sensing has been performed. Also, the interaction of this pigment with light is a comprehensive process, making researching this more feasible. Chl-a absorbs light in the visible part of the spectrum, mostly blue and red wavelengths. Absorption occurs less in green light, and light in the NIR part of the spectrum is scattered. The energy gained from light absorption is used for oxygenic photosynthesis. Algae growth is often associated with stagnant water, but it also occurs in present in rivers. Chl-a was

also selected as it can have a big impact on local environment. A bloom of algae, or eutrophication, brings unpleasant odours to the surrounding area, decrease the light penetration in water, and, in some cases, can release toxins. The decomposition of the dead algae removes dissolved oxygen from the water. When this occurs, too much oxygen is removed from the water, making the water inhabitable for aquatic life (Bhateria & Jain, 2016). Such algae bloom is parked by an overabundance of nutrients. In flowing water, primarily phosphorus and nitrogen are nutrients that induce an autotrophic state (Dodds, 2006). These nutrients occur in the water naturally, but an overabundance is often human induced, for example with the use of fertilizers which seep through the groundwater to the river.

Water quality of rivers must be approached differently than that of lakes, estuaries, and coastal regions. Rivers have freshwater that moves in one direction along its banks, and the depth of rivers is generally rather limited compared to larger bodies of water. Along the course of the river, water quality can change due to inflow of tributaries, or discharge or leaching of pollutants. This makes that the water quality at one point of the river could be very different than the quality further downstream. The (limited) mixing of input of tributaries can cause a horizontal or vertical stratification, causing changes in water quality along the cross-section of a river. Lakes are stagnant bodies of mostly fresh water. Lakes itself differ from each other and can be classified based on their chemistry, salinity, and nutrient content (Bhateria & Jain, 2016). The last one determines the productivity of a lake. Eutrophic lakes have excessive nutrients, which enables them to support an abundance of either aquatic plants or algae, but also put them at risk of eutrophication. Within a lake, water properties and quality can highly differ spatially. Normally 4 distinct zones can be identified that provide different ecological niches (Bhateria & Jain, 2016); the littoral zone, the shallow, nutrient-rich water near the shore; the limnetic zone, the layer of open-water with sufficient sunlight; the profundal zone of deep, cooler water not penetrated by sunlight and with limited dissolved oxygen; and finally, the benthic zone, the deepest zone located at the bottom of the lake. Water quality in rivers can highly differ between such zones. Estuaries and coastal regions can have various levels of salinity due to the influx of fresh water from rivers. Where the movement of water is almost absent in lakes and in one direction as in rivers, movement in estuaries and coastal areas is versatile, caused by waves, tides, bathymetry, river influx, and currents. This makes that water quality can vary at each location and depth, also enabling the support of different ecosystems.

1.2. Water quality monitoring

Monitoring river water quality is necessary to ensure the safe usage of water and to protect the environment. The gathering of local water quality data and building of a dataset enables a long-term analysis where seasonal patterns can be detected as well as individual anomalies. The more frequent this monitoring is performed, the more accurate an analysis can be. Most countries have a legal framework for water management that includes the legal limits of water quality parameters for all types of surface water bodies, and the responsible parties for and methods of water quality monitoring. The "Directive 2000/60/EC of the European Parliament and of the Council establishing a framework for the Community action in the field of water policy" (European Parliament, 2000), or Water Framework Directive (WFD), has set the standards for water quality and monitoring for all members of the European Union. The WFD and the later amendments to the directive identify the types of water bodies, define the “healthy” biological and chemical conditions of such water bodies, and outlines the water quality monitoring. This WFD serves as a blueprint for the water quality monitoring and management of all European member states, such as the Netherlands.

Dutch water legislation is based on the frameworks set out in the WFD and supplementary EU frameworks on water management, ground water quality, and water pollution. In the Netherlands,

these responsibilities are divided over several governmental bodies (Rijksoverheid, n.d.). The national government is responsible for water quality monitoring of the larger lakes, rivers, and channels. The water boards are responsible for covering regional bodies of waters. Lastly, the provinces oversee ground water monitoring. On behalf of the national government, Rijkswaterstaat, the Directorate-General for Public Works and Water Management of the Dutch Ministry of Infrastructure and Water Management, conducts this monitoring. The locations, parameters, sampling methods, frequency, and analysis methods are described in the "protocol monitoring en toestandsbeoordeling oppervlaktewaterlichamen KRW", or the "protocol for monitoring and condition assessment surface waterbodies WFD" (Rijkswaterstaat, 2020). The Netherlands is the basin of the Ems, Rhine, Meuse, and Scheldt rivers. According to the protocol (Rijkswaterstaat, 2020), the main streams of these rivers are not subjected to chl-a concentration measurements until they reach the coast. Lakes, channels, estuaries, deltas, and coastal waters are subjected to chl-a monitoring at least once a year. Chl-a concentration is measured through the analysis of water samples. Samples are taken, depending on the water depth, with a rosette system, extended sampling tubes, or bottles. Sampling at estuaries, deltas, salt lakes, and coastal waters require multiple samples at multiple sites on a line, with enough samples to form a depth profile at each site. In channels, and brackish and fresh lakes, sampling at least one site is required, comprising of the average value of at least two samples at various depths. These methods of chl-a concentration monitoring are labour intensive and require a lot of resources. Samples have to be gathered manually, and boats or ships are needed for sampling at estuaries, deltas, salt lakes, and coastal waters. Part of this work could be relieved if the chl-a monitoring was be performed remotely, namely through satellite remote sensing. With satellite remote sensing, chl-a monitoring could also be extended to areas where up until now, the monitoring was not deemed feasible or beneficial. Rijkswaterstaat has experience with pilots mapping algae growth in the North Sea using satellite imagery. Earth observation does not yet replace the in-situ sampling with ships, but a pilot is now being conducted where in-situ and remote sensing monitoring is done simultaneously for 3 years to assess the suitability of remote sensing for monitoring algae growth in the North Sea (Rijkswaterstaat, 2021).

Another example of national water legislation can be found in Serbia. The monitoring of surface water quality in Serbia is determined by national law in the 'Decree on determination of the annual monitoring program water status for 2018' (Uredbu o utvrđivanju godišnjeg programa monitoringa statusa voda za 2018). This decree determines the parameters, location, frequency, and methods of water quality analysis for all freshwater bodies in Serbia, which in turn is executed by the Environmental Protection Agency of the Serbian Ministery of Environmental Protection (Agencija za zaštitu životne sredine, Ministarstvo zaštite životne sredine). The Environmental Protection Agency has three water quality monitoring stations at the Danube-Sava confluence (Environmental Protection Agency, 2020), which is the area of interest for this research. One station is upstream of the Danube, located just before the confluence. The second station is located upstream of the Sava. The third station is located downstream of the confluence of the Danube and the Sava. One measuring station near Smederevo, further downstream of the Danube and outside of the research area, also belongs to this network. Sampling is performed at a single point in the river, 50cm below the water surface (Environmental Protection Agency, 2020). Every 1 to 2 weeks, a water quality report is published, including a variety of physical, chemical, biochemical, and organic parameters. Unfortunately for this research, these reports do not include chlorophyll-a concentrations.

1.3. Water quality monitoring through remote sensing

Satellite remotes sensing has a wide range of applications, one of which is studying properties of surface water. Most of this research has been performed on large bodies of open water, like oceans, seas, estuaries, lakes, and reservoirs, as this allows the use of most common satellites that have a

larger spatial resolution (A. G. Dekker, 1993; Gholizadeh et al., 2016; Neil et al., 2019). Surface water and its constituents can be studied through remote sensing by looking at the inherent optical properties of water constituents, namely the scattering, absorption, and optical volume scattering (A. G. Dekker, 1993). What inherent optical properties at what wavelengths should be studied depend on the parameters or constituents of interest. (A. G. Dekker, 1993) showed that chl-a absorbs light most dominantly in the red region of the spectrum (676nm), with scattering, or reflecting, of green light (550nm). Most prominent is the scattering in the NIR region (700nm) (Gitelson, 1992).

There is an inherent relation between the concentration of a constituent like chl-a and its absorption and scattering (A. G. Dekker, 1993; Gitelson, 1992; Gurlin et al., 2011; Menken et al., 2006; Mishra & Mishra, 2012). This relation is the foundation of estimating the concentration of chl-a in water. A prominent absorption at a wavelength indicates a higher concentration of a set constituent. The reflectance at a wavelength of high scattering by a constituent should not variate much with higher or lower concentrations of set constituent. Vital for establishing such a relationship is that no other constituents affect the absorption or reflectance at the wavelengths researched. CDOM has the most prominent absorption in the blue and green part of the spectrum, but also absorbs light in the red and NIR regions (Mishra & Mishra, 2012), which in theory could affect the relationship of the reflectance at these wavelengths with chl-a concentration. When researching chl-a concentration using its absorption and reflectance peak, Mishra & Mishra (2012) assumed that the absorption at of CDOM at these wavelengths would be of similar magnitude, not affecting the relationship with chl-a.

Where there has been extensive research to applying these techniques on large water bodies, only little research exists on applying this to rivers. This concept has been applied using hyperspectral airborne sensors (Olmanson et al., 2013; Shafique et al., 2003), and using satellite systems is the next step logical step. A start has been made, for example by Kuhn et al. (2019), using Landsat-8 and Sentinel-2 products to estimate chl-a concentration and turbidity on large Amazon, Columbia, and Mississippi rivers. Also Prasad et al. (2020) made progress in estimating chl-a of the Upper Ganga River, using different band-ratios using Landsat-8 bands. Applying such methods of satellite remote sensing to rivers could offer a wide range of solutions to problems concerning water quality estimations. Various water quality parameters of river water, among which chl-a concentration, could be estimated using hyperspectral, medium-high resolution satellite imagery. PRISMA (Agenzia Spaziale Italiana, 2020), a satellite launched in 2018 by Agenzia Spaziale Italiana (Italian Space Agency), or ASI, offers the opportunity to estimate these parameters in smaller water bodies, like rivers, with its 30m spatial resolution and its 238 spectral bands. Such estimations could be performed remotely and automatically. The product of such estimation would be a distribution map of a set water quality parameter, covering more area of the river in a single moment than any in-situ analyses could perform. It would enable entities to perform the required water quality monitoring using only little resources. It could also offer national and international governmental bodies the opportunity to verify water quality data if monitoring is performed insufficiently or completely lacking. Possible sources of river water constituents or pollution could be deduced from these estimations as well. This would improve strategies for water management, enable a better enforcement of water legislation, and prevent pollution.

There are drawbacks as well to using satellite remote sensing for water quality monitoring that are taken into consideration in this research. Where in-situ sampling offers the opportunity to measure water quality parameters at various depths, remote sensing allows to estimate only an average concentration of the top column of a water body. It must be considered that other constituents could significantly affect the reflectance of the wavelengths of interest. Implementing satellite remote sensing water quality monitoring would have practical limitations, the data continuity is easily

compromised. Satellite image acquisition is highly dependent on good weather. Any malfunctions of a satellite system are sometimes not easily solved, and comparable, replacing satellite systems are scares (Schaeffer et al., 2013). It is a labour-intensive process to acquire sufficient data to perform a satisfactory calibration and validation before a method can be widely applied to river water quality estimations under various circumstances. Such factors could cause policy makers and managers hesitant in implementing a remote sensing water quality monitoring system (Schaeffer et al., 2013).

1.4. Aim of the research

All in all, there is still much to learn on applying remote sensing water quality monitoring on rivers. The improvement of spatial and spectral resolution of satellite systems offers the opportunity to explore this. It is clear there is a need for it, as public health, effects of climate change, and a sustainable use of natural resources are topics that become more important by the day. The aim of this research is to investigate how suitable medium spatial resolution hyperspectral PRISMA imagery can be used for estimating and monitoring water quality of rivers and at what accuracy. This aim can be divided into 4 research questions:

1. How accurate can existing chl-a concentration algorithms be used to estimate the concentration of the Danube/Sava confluence from hyperspectral imagery?
2. How do the results improve when these algorithms are calibrated with local training data?
3. To what extend can sources or chlorophyll-a be deduced from spatial patterns?
4. To what extend would the methods used in this research be suitable for establishing a long-term water quality monitoring system?

2. Methods and data

This chapter describes necessary background information, the methods used, and the data needed for this research. This chapter follows the steps largely in the order that were taken in this research. The choice of research area, the Danube-Sava confluence, is substantiated and further details on the area is provided. The operational history of the PRISMA system is provided, as well as the technical details of the system and the available imagery of the research area. After this, the location, methods, and data of the in-situ water quality measurements are discussed. Next, two models used for the chl-a concentration estimation are explained. Image analysis is the next stap in the methods, as this describes the preparation of the PRISMA images used and the extraction of the reflectance data needed for the calibration and validation step. In this step the methods are discussed for the validation of the original models and the recalibration and validation using the local dataset. This chapter ends with the explanation on how the chl-a distribution maps were produced with resulting algorithms.

2.1. Research area

The area chosen for this research is the confluence of the Danube and Sava rivers in Belgrade, Serbia (*Figure 1, 2 and 3*). The research area is limited by the size of the PRISMA images, as these images cover an area of 30x30km. The Danube is one of the longest rivers in Europe and with one of the highest discharge volumes. To enable the analysis of PRISMA images with its 30m spatial resolution and offer the opportunity to detect spatial patterns of chl-a, rivers must have a sufficient width. The average width of the Danube in Belgrade is 550m (Drazic et al., 2014), which is more than sufficient for this research. There are multiple smaller and larger river islands in the Danube, the two most notable within the research are located in the bend in the east of the research area. Forkontumac and Čakljanac that split the Danube up in 3 streams. An approximate 45km stretch of the Danube is included in the research area, starting, just downstream of the village Novi Banovci, in the west. Downstream, the Danube leaves the research area near the village of Ritopek. Both before and after the confluence, several bridges cross the Danube. The Sava is one of the tributaries of the Danube, with an average width of 200-300m before the confluence (Drazic et al., 2014). This makes the Sava suitable for analysis with PRISMA imagery, but it limits the opportunity to detect spatial patterns. It enters the research area at the bottom of the image, near the village Ostružnica, following its course northward. After 17km the Sava joins the Danube, where the confluence of the two rivers is marked by another large river island, Great War Island. Both the Danube and Sava are used for inland shipping. Both rivers are used to discharge wastewater from the city, both treated and untreated. These are sources of pollution that have an extra focus in this research.

Figure 1 RGB PRISMA image of the research area (26-9-2021).

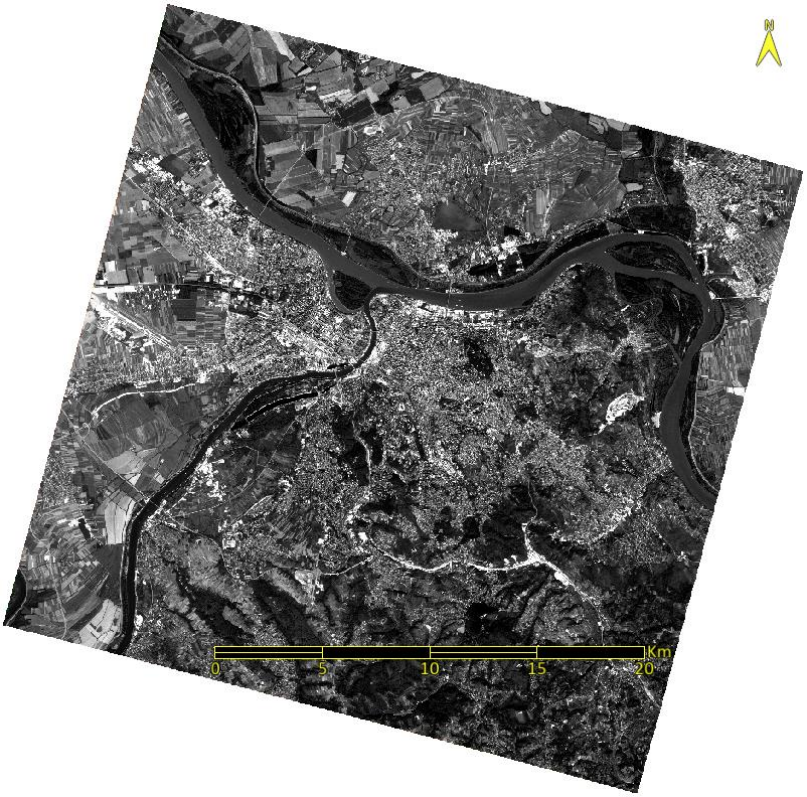

Figure 2 Panchromatic RPISMA image of the research area (26-9-2021).

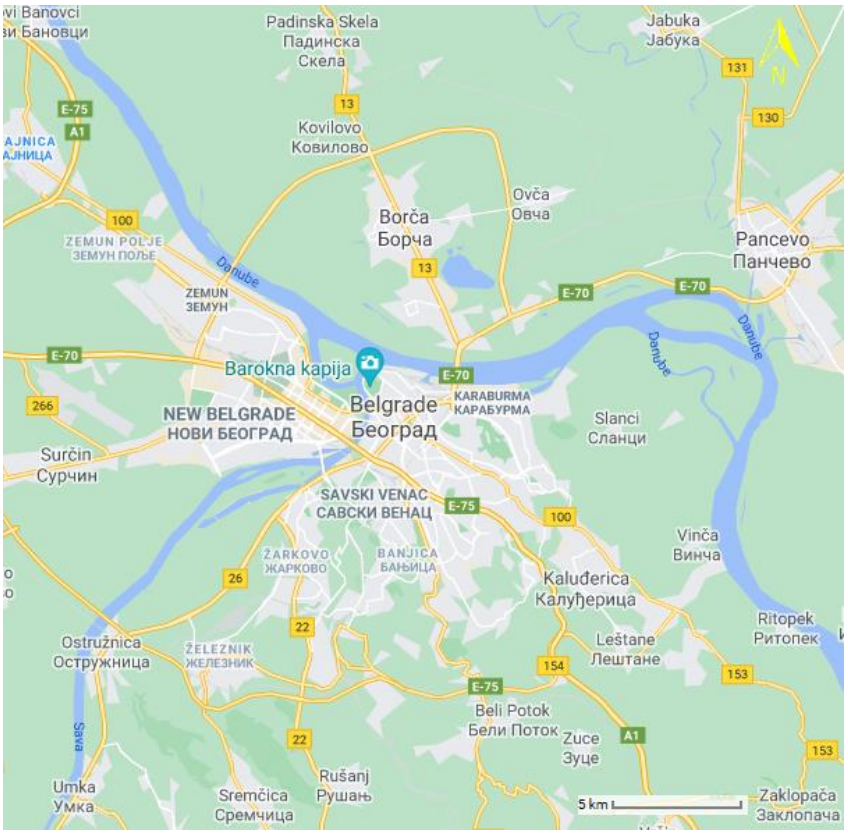

Figure 3 Map of research area (Google Maps, n.d).

The Danube-Sava confluence was chosen for this research for several reasons. Firstly, the confluence was chosen because the Danube and Sava are wide rivers. PRISMA has a spatial resolution of 5m for the panchromatic band and a 30m resolution for the VNIR and SWIR bands. Mixed pixels at the banks of the rivers are unusable for analysis, resulting in less water surface area to analyse. A wider river would offer the opportunity to distinguish spatial patterns in chlorophyll-a concentration and possibly deduce sources of direct discharges of chl-a or other forms of water pollution. This is the case for the Danube, with an average width of 550m. Analysis of the Sava, with its 200-300m width, would benefit of an even higher spatial resolution than 30x30m. Still, including the Sava enables to assess this method on a narrower river than the Danube. The confluence of the rivers lays the ground for the second reason this area was chosen. A confluence brings together two rivers with two expected different water qualities. It is expected that this would form spatial patterns and a different average chlorophyll-a concentration before and after the confluence. Lastly, and most importantly, this area was chosen because there was the possibility to have water quality measurements taken on the same moment as a PRISMA image acquisition.

2.2. PRISMA imagery

2.2.1. PRISMA

In 2019, PRISMA was launched by the Agenzia Spaziale Italiana (Italian Space Agency), or ASI, a satellite with medium-resolution hyperspectral sensor (Agenzia Spaziale Italiana, 2019). This satellite has been fully operational since October 2019. PRISMA images are acquired only on the request of users. After registering as a user with ASI, it is possible to request new images, and access any previously acquired images from other users. PRISMA imagery has a 30m spatial resolution for its VNIR and SWIR bands, and a 5m spatial resolution for its pan-chromatic band (*Table 1*). The resulting images cover an area of 30x30km. A distinct feature of PRISMA are the abundance of spectral bands and the narrow band with. There are 66 bands in the VNIR channel and 171 bands in the SWIR channel, all themselves with a band

width of ≤ 12nm. PRISMA has a sun synchronous orbit with a return cycle of 29 days (ITC, n.d.), but with adjustments of the sensor, it is possible to acquire images of locations with a 7-to-10-day interval.

Parameter	VNIR	SWIR	Panchromatic
Spectral range	400-1010nm	920-2505nm	400-700nm
Band width	≤12nm	≤12nm	-
Number of spectral bands	66	171	1
Swath width	30km		
Spatial resolution	30m		5m

Table 1 Properties of PRISMA (Agenzia Spaziale Italiana, 2020).

Compared to other systems, like Landsat 7 (USGS, 2019a) and 8 (USGS, 2019b), Sentinel-2 (European Space Agency, 2015), and MERIS (European Space Agency, 2006), PRISMA was best suited for this research. PRISMA is unique in its medium spatial resolution, narrow band widths and its high number of bands. The spatial resolution of PRISMA of 30m for the VNIR and SWIR channels is comparable to Landsat 7 and 8, both having 30m resolution. Sentinel-2 exceeds in spatial resolution, with a 10m resolution. MERIS has a 300m resolution, which is too high for the analysis for rivers. A high spatial resolution, as discussed, is required to be able to do research on narrow water bodies like rivers. What distinguishes PRISMA from the other systems, and what is vital for this research, is the abundance of spectral bands and the high spectral resolution. For the VNIR channel, which is extremely important for water quality mapping (A. G. Dekker, 1993), Landsat 7, 8, Sentinel-2 and MERIS have 4, 5, 8 and 15 bands respectively, while PRISMA offers 66 bands. A spectral resolution of ≤12nm also outclasses Landsat 7 (60nm to 130nm), 8 (2nm to 60nm), Sentinel-2 (15nm to 106nm), but not all bands of MERIS (2.5nm to 20nm). This high number of spectral bands and high spectral resolution are necessary to detect the reflectance and absorption peaks of chl-a. The fact that new PRISMA images are acquired only on request, limits the abundance and sites of already available archived images. This decreases the chance to have existing images matching with historic in-situ water quality data on date and location. Other systems have an advantage, as they are longer operational and have a larger database of available images.

2.2.2. Pre-processing of PRISMA imagery

PRISMA images are provided pre-processed. ASI (Agenzia Speciale Italiana, 2021) provides 5 levels of processing images: Level 0, Level 1, and Level 2 (b/c/d). Level 0 (L0) images consist of unprocessed data. Level 1 (L1) images underwent spectral and radiometric corrections for both the panchromatic and hyperspectral channels. These images depict the Top of the Atmosphere (TOA) spectral radiance. In addition, these images are provided with auxiliary and thematic maps like a cloud mask, sun-glint mask, and a surface classification map. Level 2 (L2) images are the outcome of further processing of L1 images and are divided in: spectral radiance at the surface (L2b), at-surface reflectance (L2c), and geocoded at-surface reflectance (L2d). The images are georeferenced, but without ground control points (GCPs) this accuracy is up to 200m. No GCPs were available for the research area.

For this research, the L2d images have been used. The atmospheric correction and georeferencing performed by ASI were assumed suitable to work with and the use reflectance spectra makes comparison with other literature studies easier. Performing these corrections within this research was not within the scope and would increase the workload and result in a similar or lower quality outcome. The use of the at-surface reflectance enabled the use of reflectance band ratios and indexes, as was done in previous research of (Gurlin et al., 2011; Mishra & Mishra, 2012), whose methods were used

in this research. It was not possible to have in-situ irradiance or reflectance measurements accompanying the in-situ water quality measurements.

2.2.3. PRISMA imagery of research area

Several images of the research area were available at the start of this research. These only covered the confluence and the downstream part of the Danube, excluding the upstream parts of the Danube and the Sava *(Figure 4)*. For this research, new images were requested that did cover the upstream parts of the rivers, and multiple images were provided. In total there were 12 PRISMA images covering (part of) the Danube/Sava confluence that were of sufficient quality (*Table 2*). The cloud coverage of these images range between 0% and 20.7%. More images of the research area were available, but the cloud coverage in these images were deemed too high to perform proper analysis. The usable images have been captured between 4 April 2020 and 26 September 2021, providing time-series of almost 18 months. This time series miss the period between October 2020 and January 2021. This time series allows for the analysis of differences in spatial patterns of chl-a over time. All images were acquired between 11:30 and 11:50 local time.

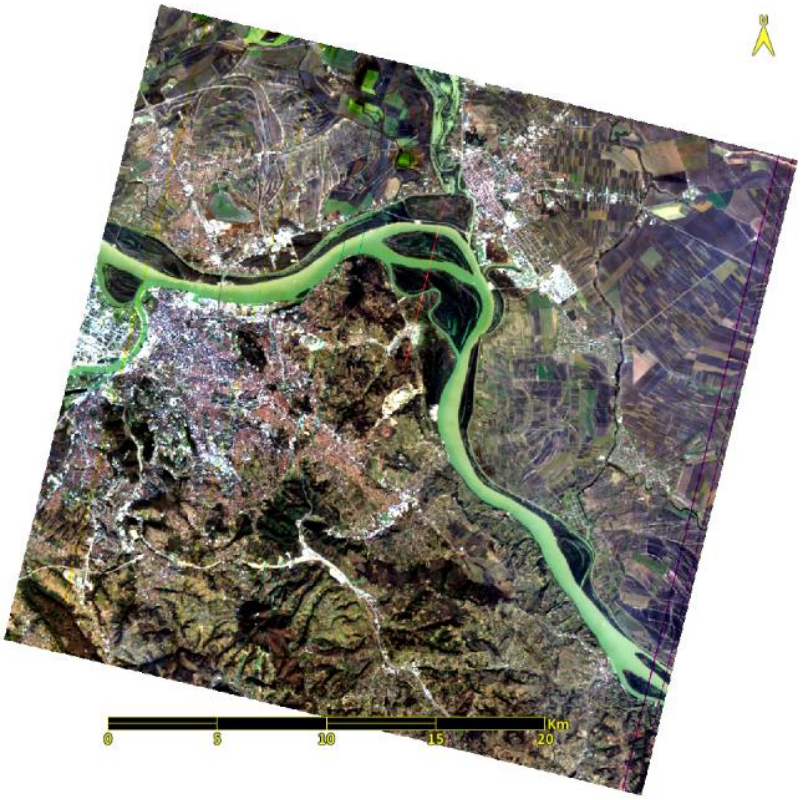

Figure 4 Example of image covering part of research area (RGB, 23-2-2021).

Date	Local time	Cloud coverage (%)	Image coverage
4-4-2020	11:37	7.0	Part of research area
25-6-2020	11:50	<1	Part of research area
24-7-2020	11:49	4.6	Part of research area
14-9-2020	11:45	<1	Part of research area
23-2-2021	11:37	<1	Part of research area
10-4-2021	11:30	<1	Part of research area
25-6-2021	11:40	<1	Entire research area
12-7-2021	11:33	0	Part of research area
4-8-2021	11:30	20.7	Entire research area
16-8-2021	11:37	0	Part of research area
3-9-2021	11:47	<1	Entire research area
26-9-2021	11:44	<1	Entire research area

Table 2 Overview of usable PRISMA images.

The image captured on 26 September 2021 (*Figure 1 and 2*) is accompanied by in-situ water quality measurements (dr. S. Kolarević, personal communication, September 28, 2021). This image has a low cloud coverage of only 0.05%, which makes it highly suitable for image analysis. This is the image that was used for applying and evaluating the original algorithms from (Gurlin et al., 2011; Mishra & Mishra, 2012), to calibrate these algorithms for this research area and to validate these calibrated algorithms. The image of 14-9-2020 was acquired approximately one year before the main image of 26-9-2021 and can be used to depict the water quality in a similar period one year prior. This image covers only part of the research, as it excludes the upstream part of the Danube and Sava. The image of 23-2-2021 covers the same research area as the image of 14-9-2021. This image was acquired approximately 7 months prior to the main image, offering the opportunity to analyse the chl-a distribution at the end of winter.

2.3. In-situ measurements

2.3.1. General

At the moment of image acquisition on 26 September 2021, a team led by Dr. Stoimir Kolarević of the Department of Hydroecology and Water Protection of the University of Belgrade Institute for Biological Research "Siniša Stanković" took a set of samples for in-situ water quality analyses. A total of 11 sites were sampled between 11:30 and 11:50 local time, where the image itself was acquisitioned at 11:44.

2.3.2. Sampling locations

The locations of the sample sites are depicted in *Figure 5* and *Table 3*. An enhanced view of the individual sites is provided in *Figure 6*. Sites 1-3 and 5-7 are located on the east-side bank of the Sava. Site 10 is located on the southside bank of the Danube, at the confluence. Sites 11, 13 and 14 are located further downstream of the Danube on its southside banks as well. Site 12 is located at a small bay, a dead river arm. Sites 4, 8 and 9 are missing from the dataset, as no sampling was performed as these sites. These sites are thus not included in this research, but the numbering of the remaining sites is not adjusted to these missing sites. Sites 1, 2, 5, 6, 12, and 13 are located in the vicinity of outlets continuously discharging minimal treated to untreated wastewater. Following is a description of every sampling site, supported by the images in *Figure 6*.

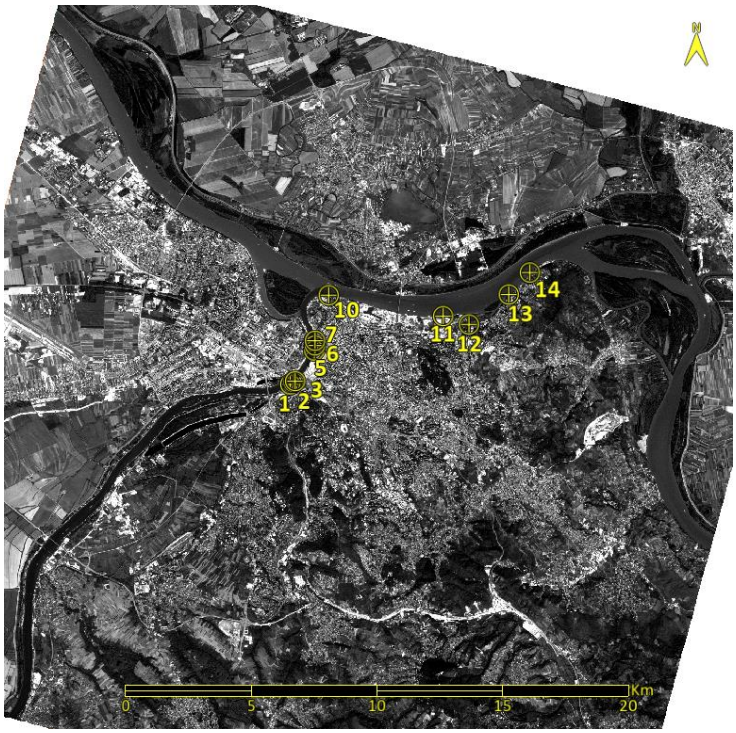

Figure 5 Overview of locations of sampling sites (Pan, 26-9-2021)

Sampling site	Site coördinates	Sampling time
1	44.798864, 20.437182	11:30
2	44.799783, 20.439051	11:30
3	44.800070, 20.439537	11:30
5	44.811445, 20.449373	11:50
6	44.812916, 20.449618	11:50
7	44.814667, 20.449640	11:50
10	44.830937, 20.456364	11:20
11	44.823844, 20.514130	11:40
12	44.820935, 20.527129	11:40
13	44.831880, 20.547474	11:40
14	44.839669, 20.557968	11:40

Table 3 Sampling locations and times.

Site 1 is located next to the New Railway Bridge (Novi železnički Most) on the upstream side. This bridge is a fully suspended bridge without pillars in the river. A sample was taken from the east-side bank of the Sava at 11:30. Several ships and floating barges are docked on the bank at the moment of sampling. An outlet of wastewater is located on downstream of the bridge. A plume with a distinctly different colour is visible originating from the outlet. The sample for this site should be representative for water quality before this outlet, taking in consideration that more outlets are located further upstream that have affected the water quality.

Site 2 is located downstream of the New Railway Bridge, downstream of the wastewater outlet. This sample was taken from the eastside bank at 11:30. The sample taken here should be a representation for water quality downstream of the wastewater outlet. Besides two floating

structures next to the bridge downstream, there are no ships or floating barges in the direct vicinity of this site.

Site 3 is approximately 50 meters downstream of site 2. A sample was taken at 11:30 as well. No floating structures are in the vicinity of this site either.

Site 5 is located on the eastside bank of the Sava downstream of the Old Sava Bridge (Stari Savski Most), a bridge that does stand with its pillars in the river. This sample was taken at 11:50 upstream of another outlet for wastewater, also visibly causing a discoloured plume. There are no boats or floating structures docked on this part of the bank.

Site 6 is located approximately 1.5km downstream of site 5, with a sample taken on 11:50 as well. This site is directly downstream of the outlet.

Site 7 is located approximately 2km downstream of site 6, also with a sample taken on 11.50. This sample is taken next to the upstream side of the Branko's Bridge (Brankov Most).

Site 10 is, located on the southside bank of the Danube, right after the confluence of the Danube and the Sava. The sample was taken 11:20 from the bank. There were no ships or floating structures docked in the vicinity of the site.

Site 11 is located downstream on the southside bank of the Danube. This sample was taken from the bank at 11:40. Here are no ships or floating structures docked either.

Site 12 is different from other sites as it is in a land-inward bay, a dead river arm with stagnant water. A wastewater outlet at the most inland part of the bay, visible from the small plume. The sample itself was taken from the end of a jetty extending into the bay at 11:40. Surrounding the sites are more jetties with smaller boats docked.

Site 13 is located downstream of the bay of site 12. This sample was taken on the southside bank of the Danube at 11:40. Upstream of this site is a smaller river island. In the stream between the mainland and the island, another outlet of wastewater is located. Besides some small docks and boats, no ships or floating structures were docked around this site.

Site 14 is located approximately 1km downstream of site 13. A sample was taken at 11:40 from the bank. Here there were no ships or floating structures docked either.

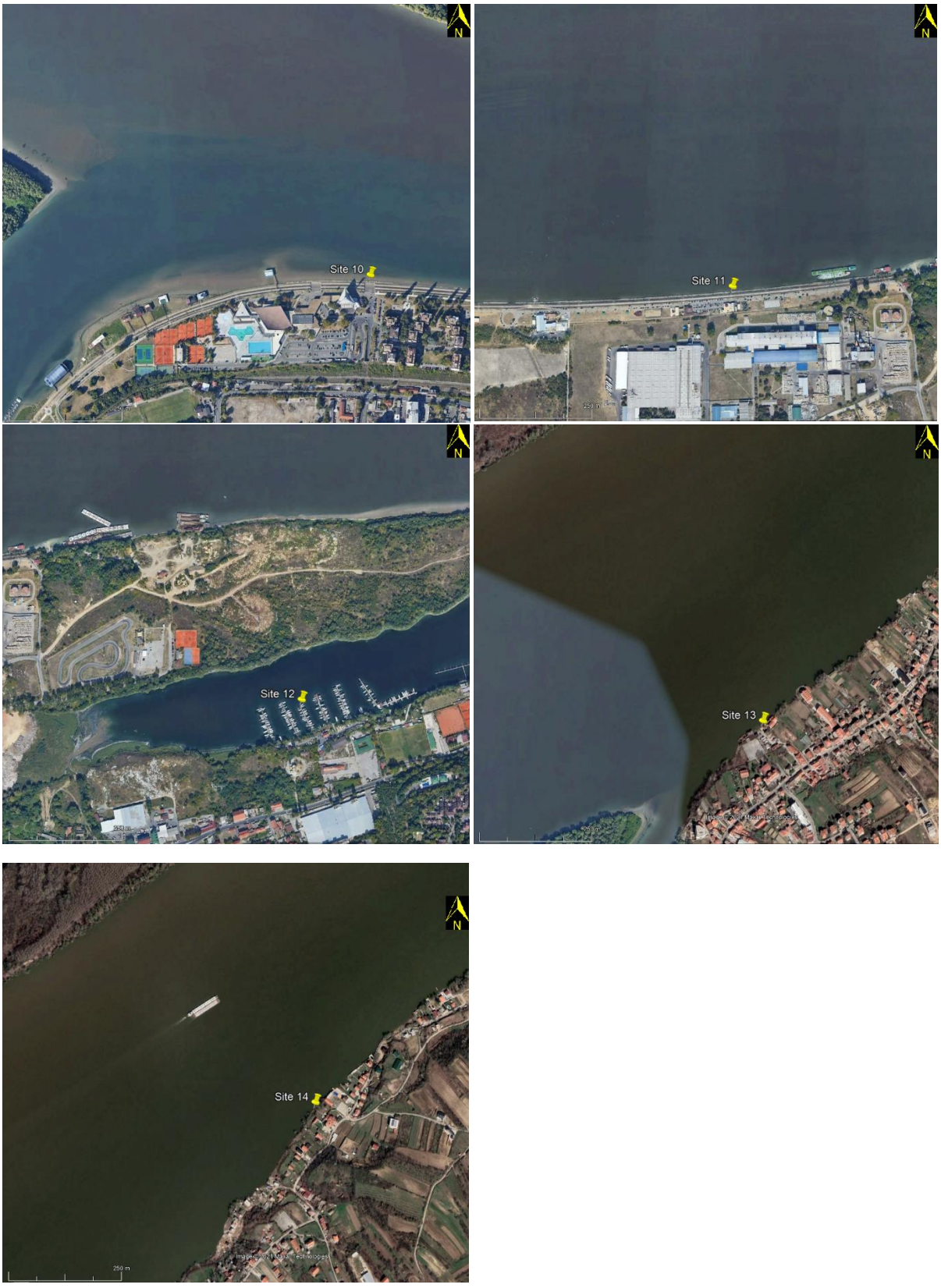

Figure 6 Locations of sampling sites 1-14 (Google Earth, n.d.).

2.3.3. Sample properties and analysis

All samples were provided with the coordinates of the sampling sites and the time of sampling. Multiple water quality parameters were analysed for each sample, included in *Table 4*. Chl-a

concentrations at the sites, the focus of this research, were measured using a YSI 6600 V2-2 sonde. These results are included in *Table 5*. With the exception of site 12, the concentrations appear to be homogenous, ranging from 2.1µg/L to 7.0µg/L. Site 12 has a chl-a concentration of 120.4µg/L and appears to be an outlier compared to the other sites. A high chl-a concentration is expected at this site though, as it is located in a bay of stagnant water with a wastewater outlet, facilitating algae growth.

Parameter	**Unit**
Temperature	°C
Conductivity	µS/m
pH	-
Total suspended solids (TSS)	mg/L
Turbidity	FAY
Chlorophyll-a concentration	µg/L
NH4-N concentration	mg/L
NO3-N concentration	mg/L
NO2-N concentration	mg/L
PO4 concentration	mg/L
Total coliform concentration	MPN/100 mL
E. coli concentration	MPN/100 mL

Table 4 Water quality parameters included in sample analysis (dr. S. Kolarević, personal communication, September 28, 2021).

Sampling site	**Chl-a (µg/L)**
1	2.3
2	5.5
3	4.2
5	2.5
6	2.8
7	2.2
10	2.1
11	3.6
12	120.4
13	7
14	4.5

Table 5 Chl-a concentrations at sampling sites (dr. S. Kolarević, personal communication, September 28, 2021).

2.4. Chlorophyll-a concentration algorithms

2.4.1. General

For this research, two algorithms for the estimation of chl-a concentrations in waterbodies were used, both in their original parameterized form and after calibration with a local dataset. The first algorithm is from Gurlin et al. (2011) and consists of a band-ratio equation using reflectance of MERIS band 7 (665nm) and 9 (709nm). The second algorithm is the Normalized Difference Chlorophyll Index (NDCI) from Mishra and Mishra (2012), which consists of an index for chl-a similar to an NDVI, using reflectance of MERIS band 7 (665nm) and 9 (709nm) as well. In their development, these algorithms were calibrated using datasets from lakes and coastal areas, with the intention to be further developed

into generally applicable models. These two algorithms were selected based on the high performance of the calibration and validation of the algorithms within these researches.

The algorithms were applied in this research in two ways, 1) in their original format, and 2) the algorithms were calibrated using the local dataset from the Danube-Sava confluence. Hence, a total of four algorithms were applied that shall be referred to as the Gurlin band-ratio algorithm, the Mishra and Mishra NDVI algorithm, or original algorithms, and the calibrated band-ratio algorithm and the calibrated NDVI algorithm, or calibrated algorithms.

2.4.2. Band-ratio algorithm

Gurlin et al. (2011) investigated the performance of a 2- and 3-band NIR-red models for the estimation of chl-a concentrations in turbid productive waters. An extensive 2008-2009 dataset from the Fremont Lakes State Recreation Area in Nebraska, USA was available for this research. This dataset contained several water quality parameters and in-situ hyperspectral reflectance measurements of 152 sites, as well as MERIS and MODIS satellite imagery. The model that proved most accurate after calibration was a two band MERIS reflection model for MERIS band 7 (665nm) and band 9 (709nm) and was deemed most promising to be developed in a general-purpose chl-a concentration calculating model for turbid, productive coastal and inland water bodies.

The widely applied reflectance ratio explained by Gitelson et al. (1985), Gitelson (1992), and Mittenzwey et al. (1991) stands at the base of the two-band model:

$$Chl - a \propto \frac{R(\lambda_1)}{R(\lambda_1)} \qquad (1)$$

where Chl-a is the chlorophyll-a concentration, $R(\lambda_1)$ is the reflectance at the reflectance peak of chl-a and $R(\lambda_2)$ is the reflectance at its absorption peak. It was shown that these wavelengths are inherently linked to the chl-a concentration. This model makes use of wavelengths in the red part of the spectrum, where *Figure* 7 shows there is a strong absorption of chl-a, and the NIR part of the spectrum, where there is almost no absorption. Other water constituents, like CDOM, have a strong influence on the reflectance in the blue and green part of the spectrum, making it impossible to correlate wavelengths on this part of the spectrum to chl-a concentration (Dekker et al., 1991; Gitelson et al., 1985; Gitelson, 1992). Absorption by CDOM in the red and NIR part of the spectrum is minimal and of similar magnitude, minimally affecting the relationship between λ_1 and λ_2. The optimal wavelengths for λ_1 and λ_2 to be used in the models were determined using the Fremont Lakes 2008 dataset. A linear regression was performed between the observed concentration and the estimated concentrations calculated using various wavelengths of the in-situ hyperspectral reflectance measurements (Dall'Olmo & Giterson, 2005; Gurlin et al., 2011). This showed that, for the two-band model, wavelengths λ_1=713nm and λ_2=666nm had the minimal values of the standard error of the estimate (STE) and were most suited to be applied in calibrating the model to the MERIS and MODIS data.

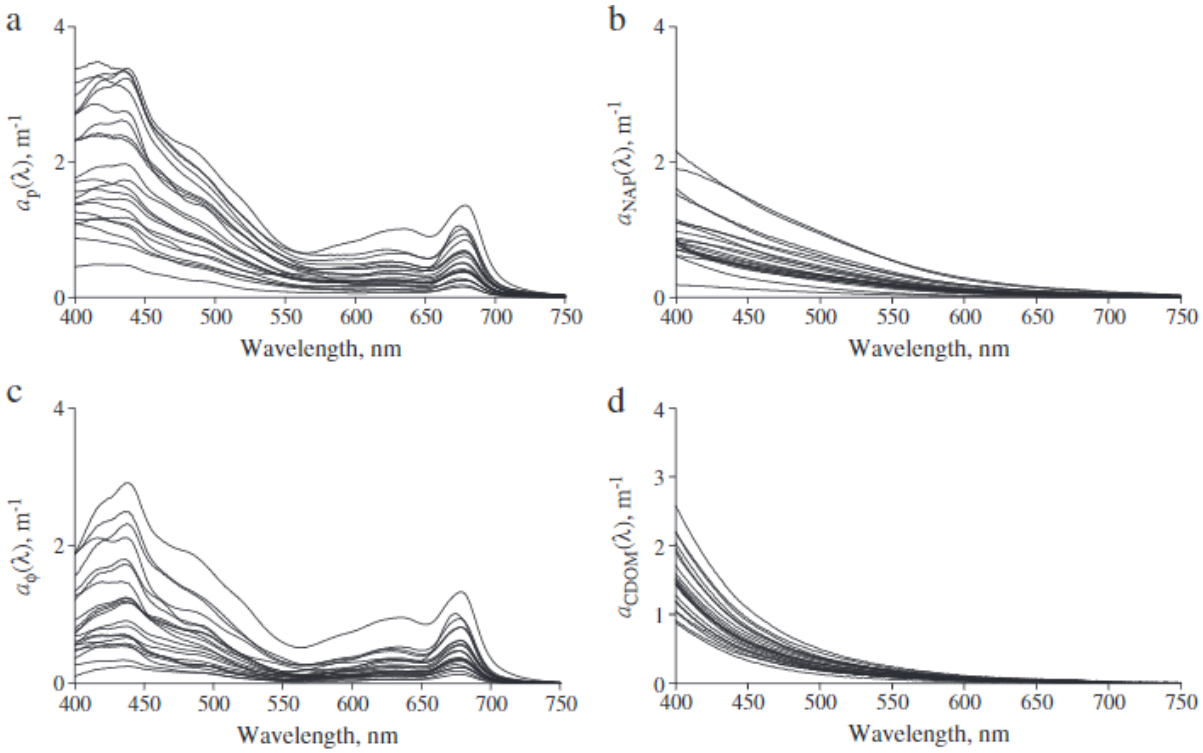

Figure 7 Representative spectra of the absorption coefficients of total particulates (a), non-algal particles (b), phytoplankton (c), and CDOM (d) for 21 water monitoring stations with chl-a concentrations from 2.3µg/L to 132.4µg/L as determined by Gurlin et al. (2011).

Using again the data of the Fremont Lakes 2008 dataset containing 89 sites and corresponding MERIS and MODIS imager, the two-band model was calibrated using a quadratic regression. The calibrated two-band model using MERIS data (*Equation 2*) showed to have the best results, with a MAE of 2.3mg/m^3 for chl-a concentrations from 0 to 100mg/m^3 and 1.2mg/m^3 for concentrations from 0 to 25 mg/m^3 (Gurlin et al., 2011).

$$Chl-a = 25.28 * \left(\frac{R(709)}{R(665)}\right)^2 + 14.85 * \left(\frac{R(709)}{R(665)}\right) - 15.18 \quad (2)$$

where Chl-a is the chlorophyll-a concentration (µg/L or mg/m^3), and R(709) and R(665) the reflectance (-) at MERIS band 9 (709nm) and band 7 (665nm). This band-ratio algorithm was also further validated Neil et al. (2019) using a dataset comprising of 2807 samples of 185 different inland and coastal water bodies, which resulted in a MAE of below 0.4µg/L and RMSE of below 1.0µg/L. Gurlin et al. (2011) showed that the MERIS two-band model has a high potential to be developed in in a simple universally applicable.

2.4.3. NDCI algorithm

Mishra and Mishra (2012) proposed a normal difference chlorophyll index (NDCI) for the estimation of chl-a concentrations in estuarine and coastal turbid productive waters. Their NDCI model performed best of the four models they evaluated. With the absence of ground truth data, this model can be used to make qualitative chl-a concentration estimations in coastal waters.

MERIS band 7 (665nm) and band 9 (709nm) were selected to formulate the NDCI:

$$NDCI = \frac{R(709)-R(665)}{R(709)+R(665)} \quad (3)$$

where the R(709) and R(665) are the reflectance (-) at MERIS band 9 (709nm) and band 7 (665nm). These two bands again represent the absorption maximum (band 7) and reflectance maximum (band 9) of chl-a. Using these bands avoided influence of CDOM and TSS on the reflectance. It was assumed that the absorption of these constituents is low and the difference in absorption between the bands neglectable. Four dataset, one modelled dataset and three and three field datasets from the MERIS satellite system, were available for this research. A modelled dataset with chl-a concentration and reflectance would offer the opportunity to review the model performance and sensitivity to a wide range of optical parameters in the water. The field datasets originated from Chesapeake Bay, Delaware Bay, the Mississippi Delta region, and the Mobile Bay, all in the US, and contained chl-a concentration observations, reflectance, solar zenith angle, and solar azimuth angle.

The simulated dataset underwent a one-fold calibration and validation. The remaining datasets underwent a three-fold calibration and validation based on three varying parameters: solar zenith angle, solar azimuth angle, and geographic region. Validation included the RMSE and the coefficient of determination (R^2) between observed and predicted chl-a. In the calibration and validation of the modelled dataset, the NDCI performed best compared to other models evaluated. The calibration resulted in the best performance parameters, with a R^2 of 0.95 and a STE of 3.62. The validation showed a RMSE of 4.83µg/L and a R^2 of 0.93. After the solar zenith angle calibration, the validation showed that the NDCI model performed well with the lowest RMSE of 1.87µg/L and an R^2 of 0.80. In the second calibration and validation for solar azimuth angle, the NDCI had a RMSE of 2.04µg/L and a R^2 of 0.48, which was second best of the six models reviewed. In the third calibration and validation, for geographical regions, the validation showed that the NDCI could predict chl-a concentration with the highest accuracy. The validation resulted in a RMSE of 1.43µg/L and a R^2 of 0.94. These results show the potential of NDCI to quantify chl-a concentration when used with remote sensing reflectance data from the MERIS satellite system.

The algorithm resulting from the calibration of the modelled dataset was selected to apply to the Danube-Sava confluence:

$$Chl - a = 314.97 * \left(\frac{R(709) - R(665)}{R(709) + R(665)}\right)^2 + 236.5 * \left(\frac{R(709) - R(665)}{R(709) + R(665)}\right) + 42.197 \quad (4)$$

where Chl-a is the chlorophyll-a concentration (µg/L or mg/m^3), and R(709) and R(665) the reflectance (-) at MERIS band 9 (709nm) and band 7 (665nm). This algorithm was selected because it had the best calibration performance measures of all four calibrations, and after validation the best validation performance measures of all six other models evaluated using the modelled dataset. As this algorithm made use of a modelled dataset, it has the highest chance it is not area-specific and has more opportunity to be universally applied. This NDCI algorithm was also further validated by Neil et al. (2019) which resulted in a MAE of below 0.3µg/L and RMSE of below 0.8µg/L.

2.5. Image analysis

2.5.1. Image preparation

Image analysis and interpretation was carried out in ENVI 5.6. This version of ENVI contained all tools necessary to analyse the image and is the only software program that has the build-in capability to read the hdf5-format PRISMA images. The L2d PRISMA images depict the at-surface reflectance and are georeferenced with an accuracy up to 200m (i.e. approximately 7 pixels). The VNIR images were used to depict a normal colour image using band 32 (651nm) for red, band 21 (555nm) for green, and band 7 (449nm) for blue. The panchromatic images were depicted in a grayscale and were used for

their higher spatial resolution. To extract reflectance of wavelengths at the sampling sites and prepare the image for chl-a estimations, the images had to be prepared.

The first step in image preparation was creating a mask for allowing the analyses of just pixels covering water. Pixels overlapping both areas of water and land, or covering bridges, large barges, or ships, either sailing or docked, could not be included in this mask. These pixels would have mixed reflectance originating from both water and the land or object, which made them unsuitable to estimate chlorophyll-a concentrations. A NDVI map was created of the image using the ENVI 5.6 NDVI-tool, in which water had a value between -1 and -0.05. A Region of Interest (ROI) was created using the tool that creates ROIs from band thresholds, containing all pixels with an NDVI between these values to cover water area. A ROI with an NDVI outside of these values was created as well to represent land and objects covering water. The ROI for water still contained pixels at the edges that partly covered the riverbanks. Hence, a buffer was created using the buffer zone for ROIs tool between the ROIs for water and land. This resulted a single line of pixels around all borders of the ROI for water could be removed. This ensured almost all mixed pixels were removed from the ROI for water. Later it did turn out this system was not able to remove all sailing ships. The final ROI for water is depicted in *Figure 8* and was used to create a mask that allowed for the analysis of the area within this ROI.

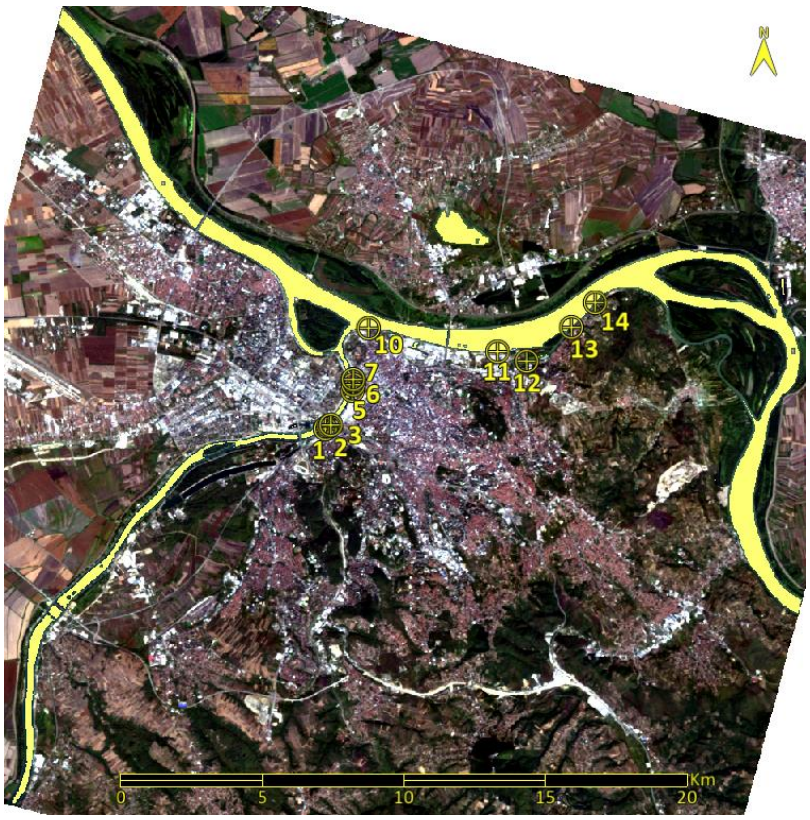

Figure 8 ROI of water (RGB, 26-9-2021).

2.5.2. Sampling site localisation and reflectance extraction

To validate the Gurlin band-ratio algorithm and Mishra and Mishra NDVI algorithm, and to calibrate and validate these algorithms with the local dataset, the reflectance of band 34 (669nm) and 38 (709nm) had to be extracted at the in-situ sampling sites. The coordinates of the in-situ sampling sites cannot be used to place these sights in the PRISMA image, as the geocoding of this image has an error of up to 200m. The sampling sites were thus located visually using the PRISMA panchromatic image and high-resolution Google Earth imagery (*Figure 6*) that did show the accurate coordinates. It was not possible to verify the accuracy with which the sampling sites were located in the PRISMA imagery.

Based on the 5m resolution of the panchromatic images and 30m resolution of the RGB images, it is estimated that the sites were in the imagery with an accuracy of one 30m pixel.

Only the areas of water within the ROI for water can be analysed, but most of the in-situ samples were taken from the banks of the river and fall outside of this ROI. To compensate for this, every sampling site was assigned a ROI of the 5 (8 for site 12) closest pixels that were within the ROI for water, the average reflectance of which would be most representable for this sampling site. What follows is an overview of every sampling site with a description of how that site's ROI was selected. These descriptions are supported by a RGB image including the ROI for water and the ROIs of the sampling sites to show the distance of the ROI for water to the actual sampling sites. Panchromatic images show the location of the ROIs of the sampling sites in higher resolution.

Site 1 was located on the bank of the Sava, between a floating structure and a bridge. Five pixels on the upstream side of the bridge that were closest to the site were selected for the ROI. This site is upstream of an outlet of wastewater; hence no pixels were selected downstream of the bridge.

Site 2 was also located on the bank of the Sava directly downstream of a wastewater outlet. In total, five pixels closest by were selected for the ROI. As this site is only 50m upstream of site 3, and to avoid the ROI extending too far out to the middle of the Sava, one pixel overlaps with the ROI for site 3.

Site 3 is 50m downstream of site 2. Five pixels were selected for the ROI, of which one overlaps with the ROI of site 2. After analysis, it turned out one of the pixels of this ROI overlaps with a bridge that was not removed from analysis during image preparation.

Figure 9 ROI of water and ROIs of sampling sites 1-3 (RBG, 26-9-2021).

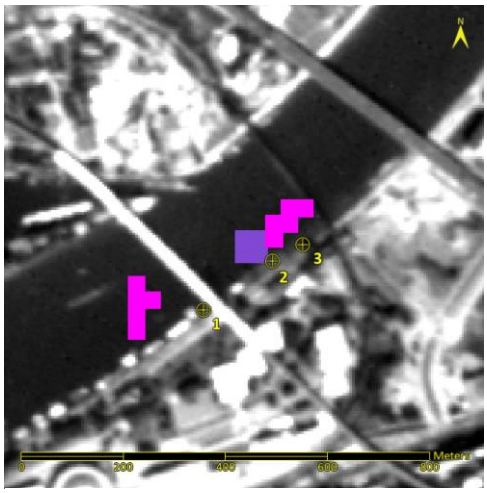

Figure 10 ROIs of sampling sites 1-3 (PAN, 26-9-2021).

Site 5 is located on the bank of the Sava too, just upstream of another wastewater discharge. Five pixels were selected for this ROI, avoiding overlap with area around the discharge site.

Site 6 is located downstream of site 5. Five pixels were selected to make up this site's ROI. This site is located just downstream of a wastewater outlet.

Site 7 is located at the foot of a bridge over the Sava, which results in unusable pixels in its direct vicinity. Five pixels were chosen both upstream and downstream of the bridge to make up the ROI.

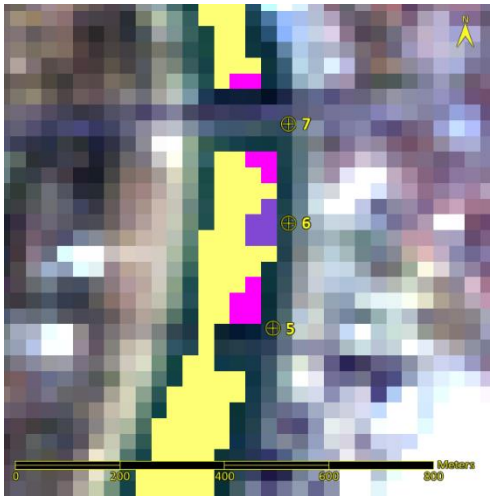

Figure 11 ROI of water and ROIs of sampling sites 7-9 (RBG, 26-9-2021).

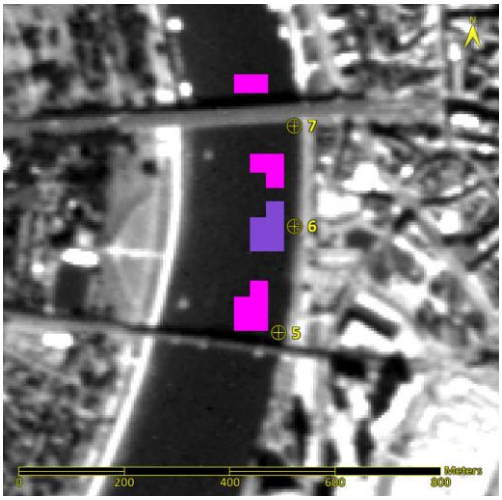

Figure 12 ROIs of sampling sites 7-9 (PAN, 26-9-2021).

Site 10 is located on the southside bank of the Danube, right after the confluence of the Danube and the Sava. Five pixels were selected closest to the site.

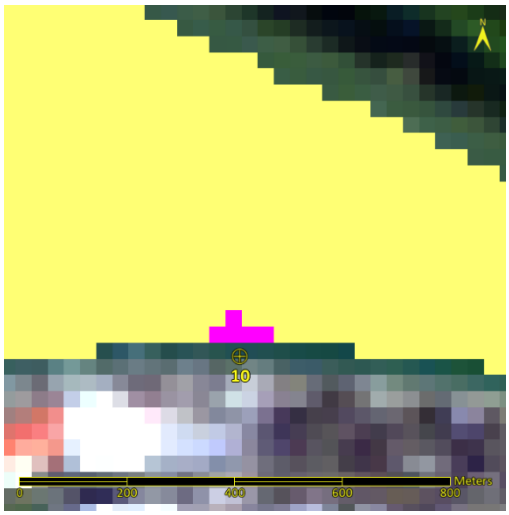

Figure 13 ROI of water and ROI of sampling 10 (RBG, 26-9-2021).

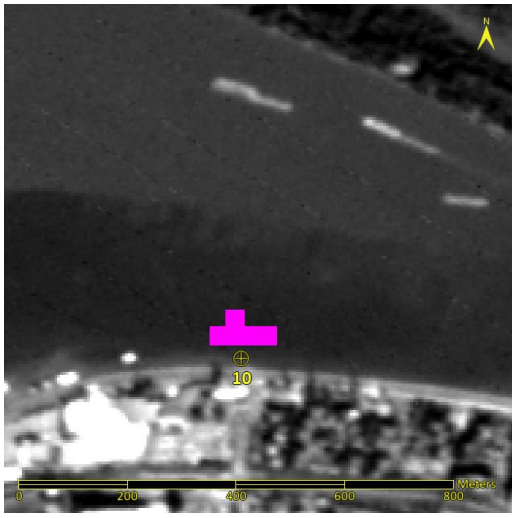

Figure 14 ROI of sampling site 10 (PAN, 26-9-2021).

Site 11 is also located on the banks of the Danube. The five closest pixels were selected for the ROI.

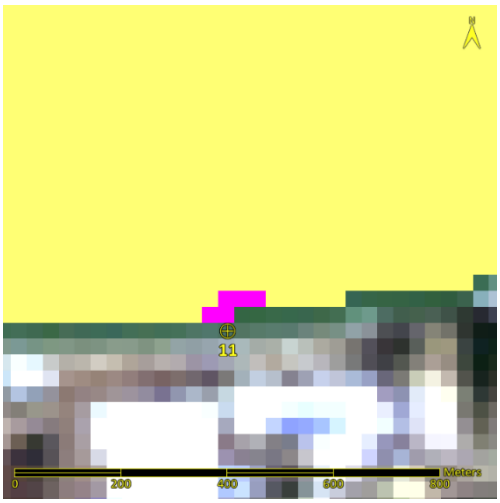

Figure 15 ROI of water and ROI of sampling 11 (RBG, 26-9-2021).

Figure 16 ROI of sampling site 11 (PAN, 26-9-2021).

Site 12 is different from the other sites. The sample is taken from a jetty in a small bay of the Danube. This bay is mostly surrounded by land, and after removing mixed pixels from the analysis, only a few pixels remained. The in-situ sample showed that the chlorophyll-a concentration of 120.4 µg/L was higher than in the Danube itself. The water in the bay is slow-moving to stagnant, and wastewater is discharged in the bay west of the sample location. Next, there is a yacht/boat harbour close to this observation point which may cause an additional influx of contaminants. There were no five adjacent pixels at or close to the site, so the eight closest pixels were chosen to make up this ROI. One pixel was located besides the sampling site but had a small overlap with one of the jetties. Other pixels were 100m to 200m away.

Figure 17 ROI of water and ROI of sampling 12 (RBG, 26-9-2021).

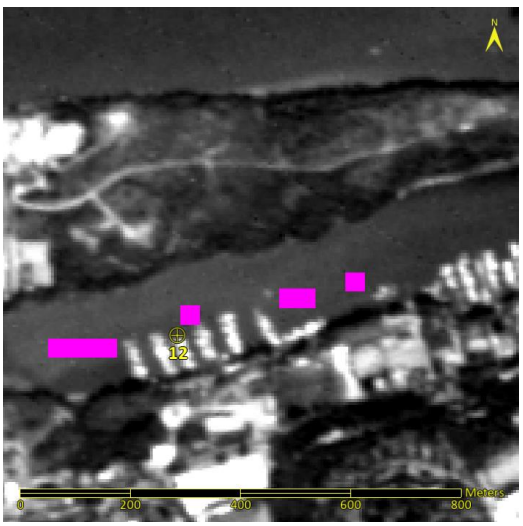

Figure 18 ROI of sampling site 12 (PAN, 26-9-2021).

Site 13 is located on the bank of the Danube downstream part of the bay. Five pixels were selected for the ROI.

Figure 19 ROI of water and ROI of sampling 13 (RBG, 26-9-2021).

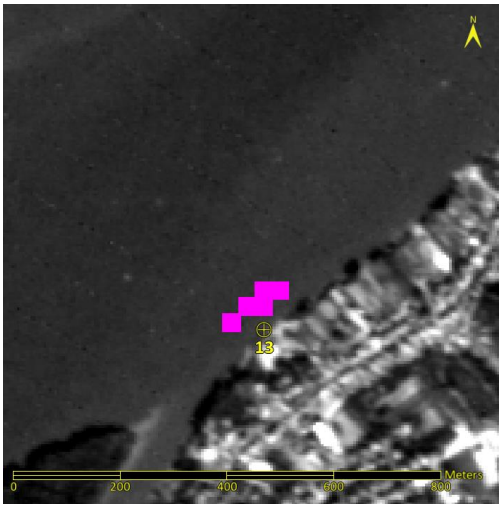

Figure 20 ROI of sampling site 13 (PAN, 26-9-2021).

Site 14 is also located on the bank of the Danube, just before large bend in the river. Five pixels selected for the ROI.

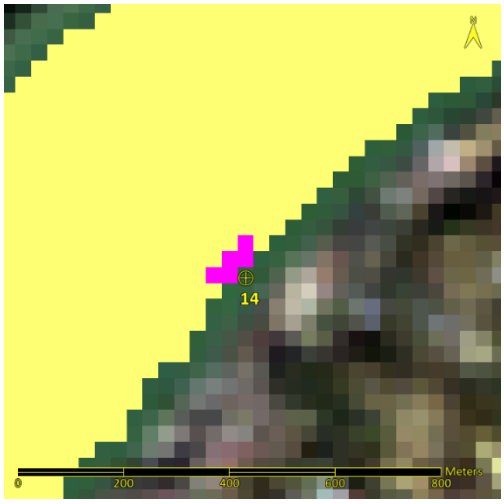

Figure 21 ROI of water and ROI of sampling 14 (RBG, 26-9-2021).

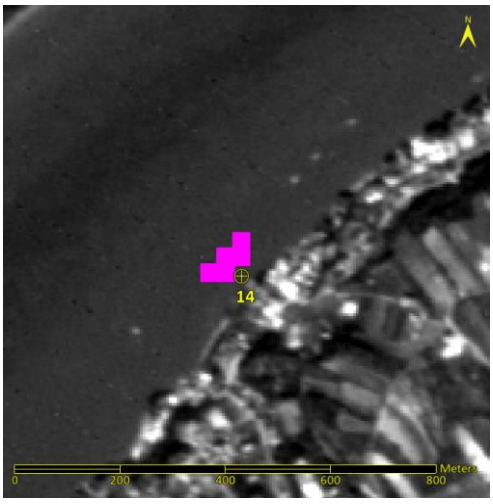

Figure 22 ROI of sampling site 14 (PAN, 26-9-2021).

The average reflectance ($\bar{R}$) of all the site's ROIs, all five or eight pixels, for band 38 (709nm) and band 34 (669nm) were extracted and are listed in *Table 6* with the Standard Deviation (SD). This data is discussed in this chapter, the *Methods and data* section, rather than the *Result* section, as it is considered and handled as initial data enabling further analysis. The SD for most average reflectance were low enough compared to the $\bar{R}$ to assume that the ROI covered a homogenous area. For some sites S3 and S12, the SD of both bands is over 10% the value of $\bar{R}$, indicating the ROI covering a more heterogeneous area. This can be caused by local differences in chl-a concentration, but also by features like floating objects that are included in within pixel a pixel of the ROI objects that affect the reflectance.

Site	Band	R̄	SD
S1	38 (709nm)	0.01204	0.0006
	34 (670nm)	0.02008	0.00112
S2	38 (709nm)	0.01268	0.00064
	34 (670nm)	0.01982	0.00055
S3	38 (709nm)	0.01467	0.00412
	34 (670nm)	0.02068	0.00232
S5	38 (709nm)	0.01254	0.00107
	34 (670nm)	0.02062	0.00113
S6	38 (709nm)	0.01178	0.00079
	34 (670nm)	0.02022	0.00109
S7	38 (709nm)	0.01261	0.00055
	34 (670nm)	0.0202	0.00074
S10	38 (709nm)	0.01203	0.00073
	34 (670nm)	0.02183	0.00089
S11	38 (709nm)	0.02271	0.00155
	34 (670nm)	0.03588	0.00179
S12	38 (709nm)	0.06596	0.00815
	34 (670nm)	0.03378	0.00397
S13	38 (709nm)	0.02175	0.00063
	34 (670nm)	0.03291	0.00086
S14	38 (709nm)	0.02104	0.00046
	34 (670nm)	0.03314	0.00071

Table 4 Average reflectance and standard deviation of site ROIs at bands 34 and 38.

2.6. Calibration and validation

2.6.1. Calibration of algorithms

The band-ratio of the two-band model of Gurlin et al. (2011) (*Equation 5*), and the NDCI from Mishra and Mishra (2012) (*Equation 6*), were calculated for each sampling sites' reflectance. To calibrate the algorithms the band-ratio and NDCI results were paired with the in-situ chl-a concentrations and separately underwent a quadratic regression. A quadratic regression was chosen as the relation between chl-a and reflectance did not prove to be linear in Gurlin et al. (2011) and Mishra and Mishra (2012), and both used a quadratic regression for calibration. Using the same type of regression enables a better comparison between the universal algorithms and the algorithms calibrated in this research. The resulting calibrated band-ratio and NDCI algorithm are presented and discussed in detail in the *Results* section.

$$Band - ratio = \frac{R(709)}{R(669)} \tag{5}$$

$$NDCI = \frac{R(709) - R(669)}{R(709) + R(669)} \tag{6}$$

2.6.2. Validation of original algorithms

The Gurlin band-ratio algorithm and Mishra and Mishra NDCI algorithm were both calibrated and validated during their development. This was done using data from large turbid, productive waterbodies, like coastal waters and lakes (Gurlin et al., 2011; Mishra & Mishra, 2012). To assess the original algorithms' applicability to rivers, they were validated using the Danube-Sava dataset. The results of the validation are included in the *Results* section. Chl-a concentrations for each site were

calculated from this dataset using the Gurlin band-ratio algorithm and Mishra and Mishra NDCI algorithm and were combined with the 11 observed concentrations. The original algorithms were plotted together with the observed concentration to visualise the working of the algorithms. For a better depiction of the algorithm in low chlorophyll-a concentrations, the algorithms were plotted with the exclusion of site 12 (120.4µg/L) as well. For validation of the algorithms, several performance measures were used set forth by (Janssen & Heuberger, 1995). The Mean Absolute Error (MAE) provides a view on the absolute misestimation of the model but is sensitive to outliers. The standardised version of the MAE is the Normalized Mean Absolute Error (NMAE), where the MAE is divided by the mean predictions of the model. The Root Mean Square Error (RMSE) was calculated, as well as the Normalized Root Mean Square Error (NRMSE). It was found that the NMAE would be the most suitable measure of all four to judge the performance of the algorithms. The NMAE depicts the absolute error relative to the observations. A larger error for an area with a high observed chlorophyll-a concentration will affect the measure less as it would for measures based on absolute values.

2.6.3. Validation of calibrated algorithms

Only 11 in-situ measurements were available for both the calibration and validation of the model of the model. The choice was made to use all this data for calibration, leaving none available for validation. Still, two methods of validation could be applied to give an indication for the performance of the calibrated band-ratio and NDCI algorithms.

To directly compare the performance of the original and calibrated algorithms, the performance was calculated using all 11 in-situ measurements as validation data. Again, the MAE, NMAE, RMSE, and NRMSE were applied (Janssen & Heuberger, 1995). As the data for this validation is the same as was used for calibration, these measures are not a proper depiction of the performance of the model and should only serve as an impression.

Another method was applied to provide an unbiased method of validation. Both the band-ratio and NDCI algorithms were calibrated again using a quadratic regression with data of only 8 in-situ measurements, leaving 3 samples for validation purposes. Samples 3, 7 and 13 were selected to serve as validation data. These 3 samples represent an average of varying sites in the dataset, with exception of site 12. The 3 sites were measured in both the Sava (sites 3 and 7) and Danube (site 13) and represent an average of the chl-a concentration range observed. Using these 3 samples, the MAE, NMAE, RMSE, and NRMSE were calculated for these so-called recalibrated algorithms. These performance measures should also be a representation of the performance of the algorithms calibrated with the full dataset. The performance measures of both the calibrated and recalibrated algorithms are included in the *Results* section.

2.7. Calculating chlorophyll-a concentration distribution

Using the four algorithms, the Gurlin band-ratio algorithm and the Mishra and Mishra NDCI algorithm, and the calibrated band-ratio and NDCI algorithm, the chlorophyll-a distribution of the entire image was calculated. The recalibrated algorithms only served for validation purposes and were not used to calculate chl-a distributions. The calculation was done using the band math tool of ENVI in combination with the mask of the river area which excluding pixels covering land and mixed pixels. The chl-a distribution is depicted in a white-green scale, with white being no to low concentration and green high concentrations. All areas unsuitable or available for analysis, like land, ships, bridges, and other forms of mixed pixels are depicted as white too. A different concentration scale was used for each algorithm, as the algorithms did not give similar results. The maximum values of the concentration scales were based on the average of the highest observed concentrations in the rivers and local spikes in observed concentration, all in all showing the most complete distribution with a clear contrast. The

concentration distributions include both the full views of the research area and zoomed in views specific areas of interest.

The chl-a distribution maps from the algorithm that showed the best performance was used to analyse the distribution and sources of chl-a. It was also used to analyse the shortcomings of these methods. The chl-a distribution of two other images of this area were calculated as well using this algorithm in support of the spatial distribution analysis. The image of 14-9-2020 was acquired approximately one year before the main image of 26-9-2021 used for calibration and validation and can be used to depict the water quality in a similar period one year prior. This image covers only part of the research, as it excludes the upstream part of the Danube, before the confluence. The image of 23-2-2021 covers the same research area as the image of 14-9-2021. This image was acquired approximately 7 months prior to the main image, offering the opportunity to analyse the chl-a distribution at the end of winter

3. Results

This section describes the results of this study and is structured as follows. The results of the calibration of the band-ratio and NDCI algorithms using local training data are depicted first. These consist of the formulas with the parameters resulting from the calibration. These are discussed first in order to review the validation of these calibrated algorithms simultaneously with the validation of the original algorithms. The validations include a plot of the algorithm together with the in-situ measurements, and the performance measures. The validations of the Gurlin band-ratio algorithm and calibrated band-ratio algorithm are shown together first and the validations of the Mishra and Mishra NDCI algorithm and calibrated NDCI algorithm second. Lastly, the resulting chl-a concentration distribution maps of these four algorithms are shown in the same order.

3.1. Algorithm calibration

3.1.1. Band-ratio algorithm

Performing the calibration of the band-ratio algorithm using the local dataset resulted in the following algorithm:

$$Chl - a = 48.308 * \left(\frac{R(709)}{R(670)}\right)^2 - 36.526 * \left(\frac{R(709)}{R(670)}\right) + 7.563 \quad (7)$$

where Chl-a is the chlorophyll-a concentration (µg/L or mg/m^3), and R(709) and R(670) the reflectance (-) for PRISMA band 38 (709nm) and PRISMA band 34 (670nm). The coefficients and constant of this algorithm are significantly different than the original Gurlin band-ratio algorithm (*Formula 2*).

3.1.2. NDCI algorithm

Performing the calibration of the NDCI algorithm using the Belgrade dataset resulted in the following algorithm:

$$Chl - a = 321.958 * \left(\frac{R(709)}{R(670)}\right)^2 + 181.818 * \left(\frac{R(709)}{R(670)}\right) + 28.216 \quad (8)$$

where Chl-a is the chlorophyll-a concentration (µg/L or mg/m^3), and R(709) and R(670) the reflectance (-) for PRISMA band 38 (670nm) and PRISMA band 34 (670nm). The coefficients and constant of this algorithm are also significantly different than the original counterpart in *Formula 4*.

3.2. Algorithm validation

3.2.1. Gurlin and calibrated band-ratio algorithm

Figure 23 depicts the Gurlin and calibrated band-ratio algorithms, as well as the observed chl-a concentrations. It covers the full chl-a concentration range of the in-situ observations, from 0 to 140µg/L. On this scale, both band-ratio algorithms seem to have a good fit with lower concentration sites, where the standard algorithm shows a slightly lower result for site 12. *Figure 24* displays a smaller scale than *Figure 23*, only covering the chl-a concentration from 0 to 14µg/L and show an indication of the algorithms' performances in a low-concentration environment. The variance in observations does not allow a perfect fit of an algorithms. Both algorithms show a general fit with the small number of samples. Mind that all observations have been used as training data for the calibration of the algorithm.

Overall, the Gurlin band-ratio algorithm shows a moderate performance algorithm (*Table 7*). A MAE of 2.02µg/L appears high in a low chl-a concentration environment, but the NMAE of 0.15 puts this into perspective. A NMAE of 0.15 means that the Mean Absolute Error is 15% of the observed concentrations. The RMSE was 3.43, with a NRMSE of 0.24.

From the performance measures of the calibrated band-ratio algorithm, it appears that it has a good performance. Nevertheless, the validation of the recalibrated algorithm shows that a poorer performance. The MAE of 0.87µg/L for the calibrated algorithm increases to 2.13µg/L in the recalibrated algorithm, which is comparable in magnitude to the MAE of 2.02µg/L of the Gurlin band-ratio algorithm. The NMAE of 0.06 increases to 0.40, and even though the MAE of the Gurlin and recalibrated algorithm were similar, the NMAE shows that the relative performance is worse. The RMSE of both the calibrated and recalibrated algorithm, 1.17 and 2.19 respectively, are lower than the Gurlin algorithm. Again, when normalized, the NRMSE of 0.49 of the recalibrated algorithms turns out higher than that of the Gurlin algorithm.

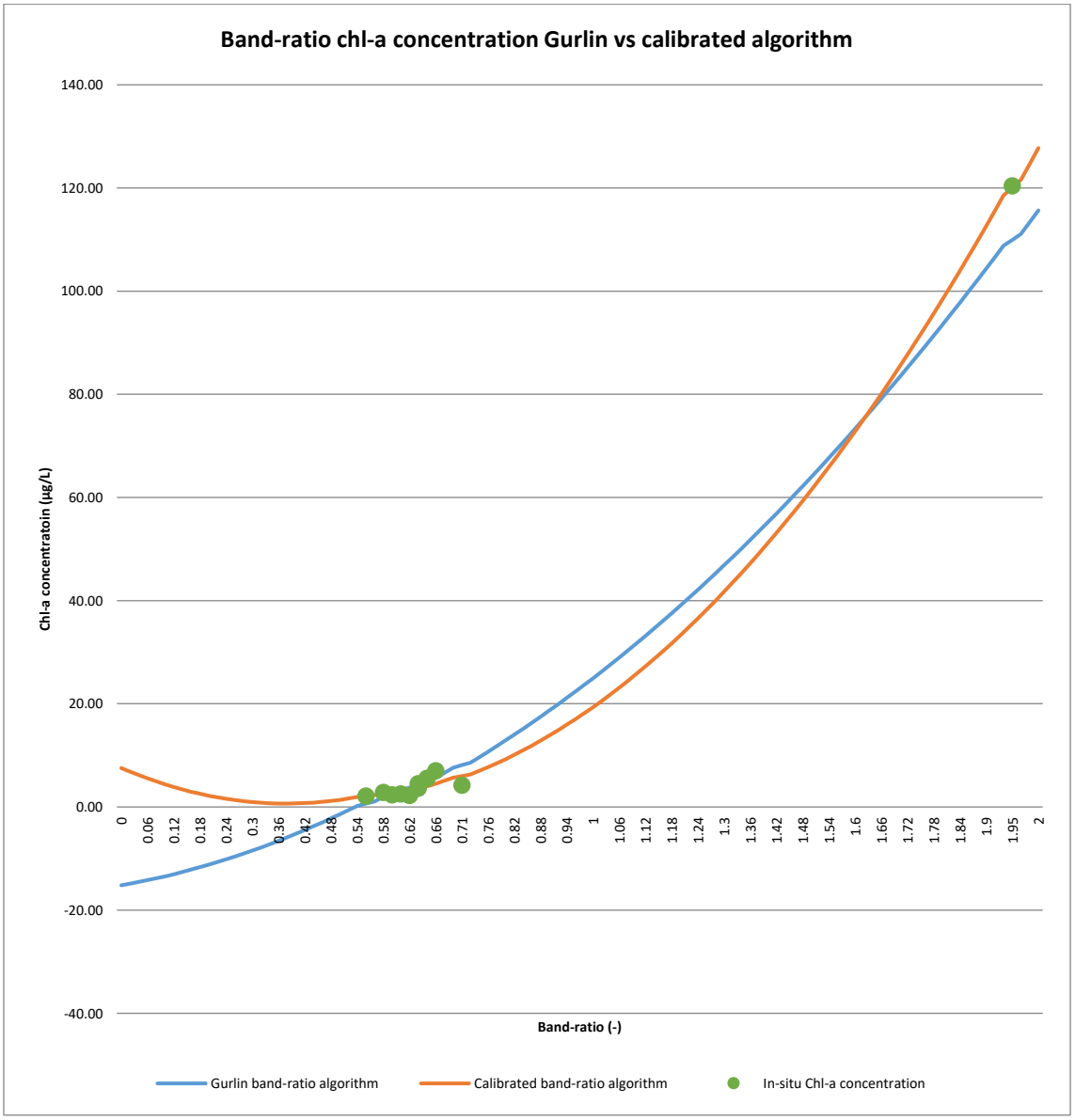

Figure 23 Gurlin and calibrated band-ratio algorithms plotted with in-situ chl-a concentrations.

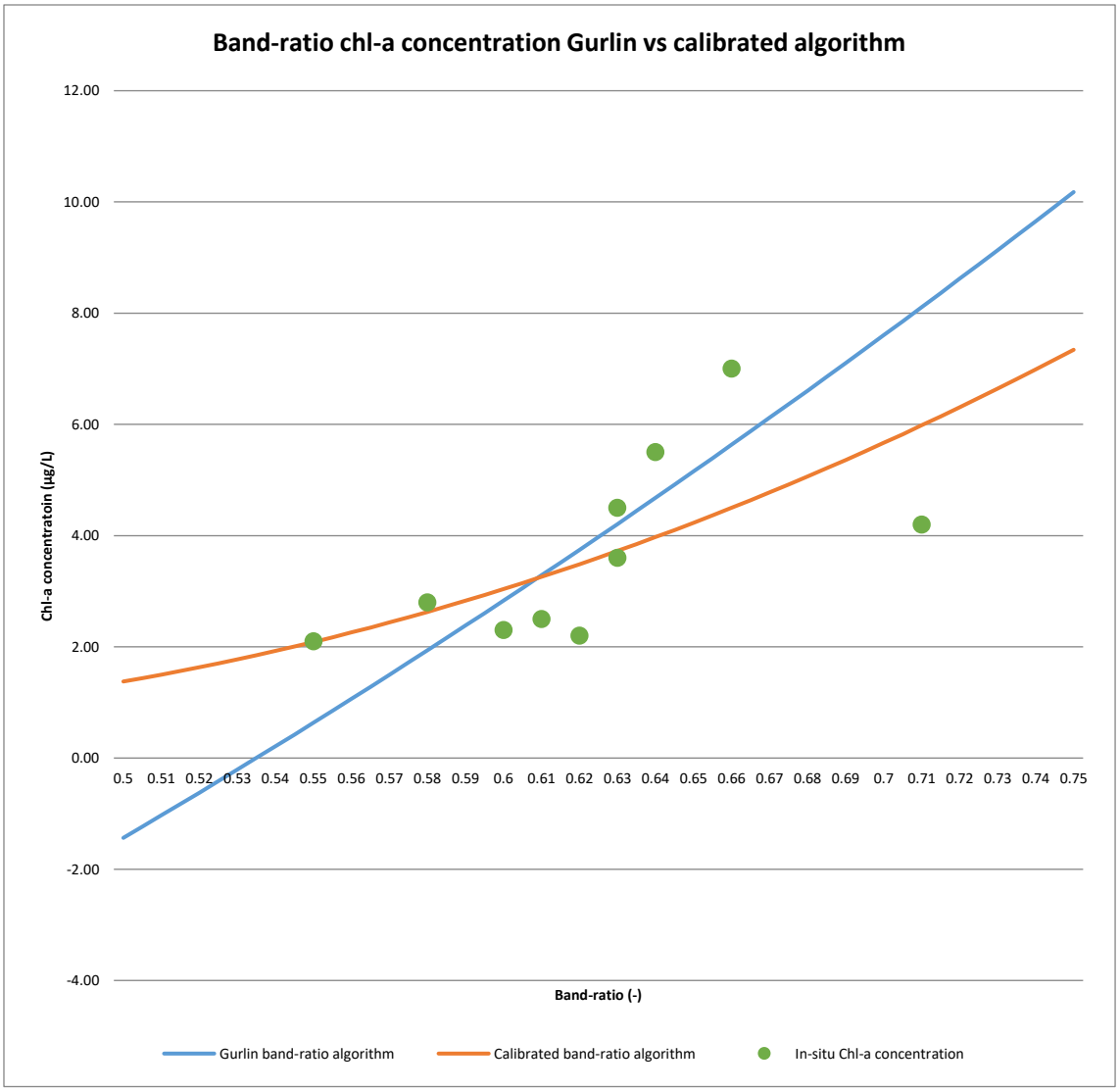

Figure 24 Gurlin and calibrated band-ratio algorithms plotted with in-situ chl-a concentrations, excluding site 12.

	Gurlin	Calibrated	Re-calibrated
MAE	2.02	0.87	2.13
NMAE	0.15	0.06	0.40
RMSE	3.43	1.17	2.19
NRMSE	0.24	0.08	0.49

Table 5 Performance measures for the Gurlin, calibrated, and re-calibrated band-ratio algorithms.

3.1.2. Mishra and Mishra and calibrated NDCI algorithm

Figure 25 shows the full available chl-a concentration range, and again both NDCI algorithms seem to form a general fit. For the high 120.4µg/L observation at site 12, the Mishra and Mishra algorithm makes an overestimation, while the calibrated variant does fit the observation. In *Figure 26*, which excludes site 12, the Mishra and Mishra algorithm shows a steeper incline in relation to the in-situ concentrations. The calibrated algorithm shows a better fit in this for the low results, again taking into consideration the use of these samples for calibration of this algorithm.

Overall, the performance measures of the Mishra and Mishra NDCI algorithm show a better result than the calibrated and re-calibrated NDCI algorithms (*Table 8*). The MAE of the general algorithm is 0.94µg/L, with a NMAE of 0.07. This NMAE is also lower than that of the Gurlin band-ratio algorithm

and only 0.01 higher than the calibrated band-ratio algorithm. The RMSE of 1.28 is low as well compared to the other algorithms, and when normalized is 0.09. This NRMSE is lower than the Gurlin band-ratio algorithm and only slightly higher than that of the calibrated band-ratio algorithm. Overall, the Mishra and Mishra NDCI algorithm showed the best performance measures of all four algorithms.

The calibrated algorithm, even with the same training and validation data, algorithm showed the poorest performance measures. When the model was recalibrated, these performance measures actually improved and were comparable with those of the recalibrated band-ratio algorithm. The MAE was 4.20µg/L and decreased to 2.29µg/L after recalibration. The NMAE was 0.23 and increased to 0.41, which is only 0.01 lower than its band-ratio counterpart. The calibrated NDCI algorithm had a high RMSE of 9.60, which decreased to 2.48 after recalibration. When normalized, the NRMSE were 0.67 and 0.55 respectively.

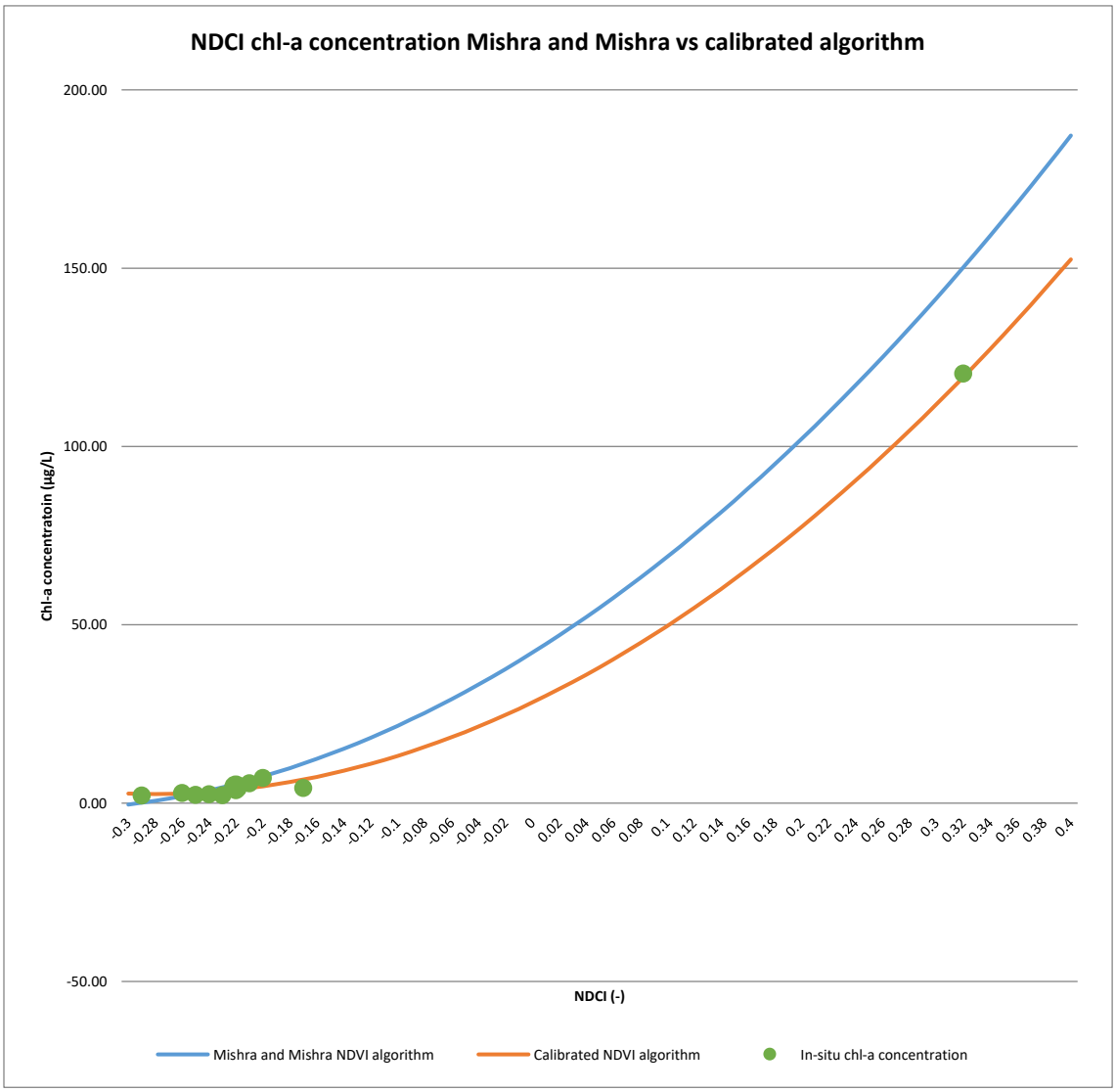

Figure 25 Mishra and Mishra and calibrated NDCI algorithms plotted with in-situ chl-a concentrations.

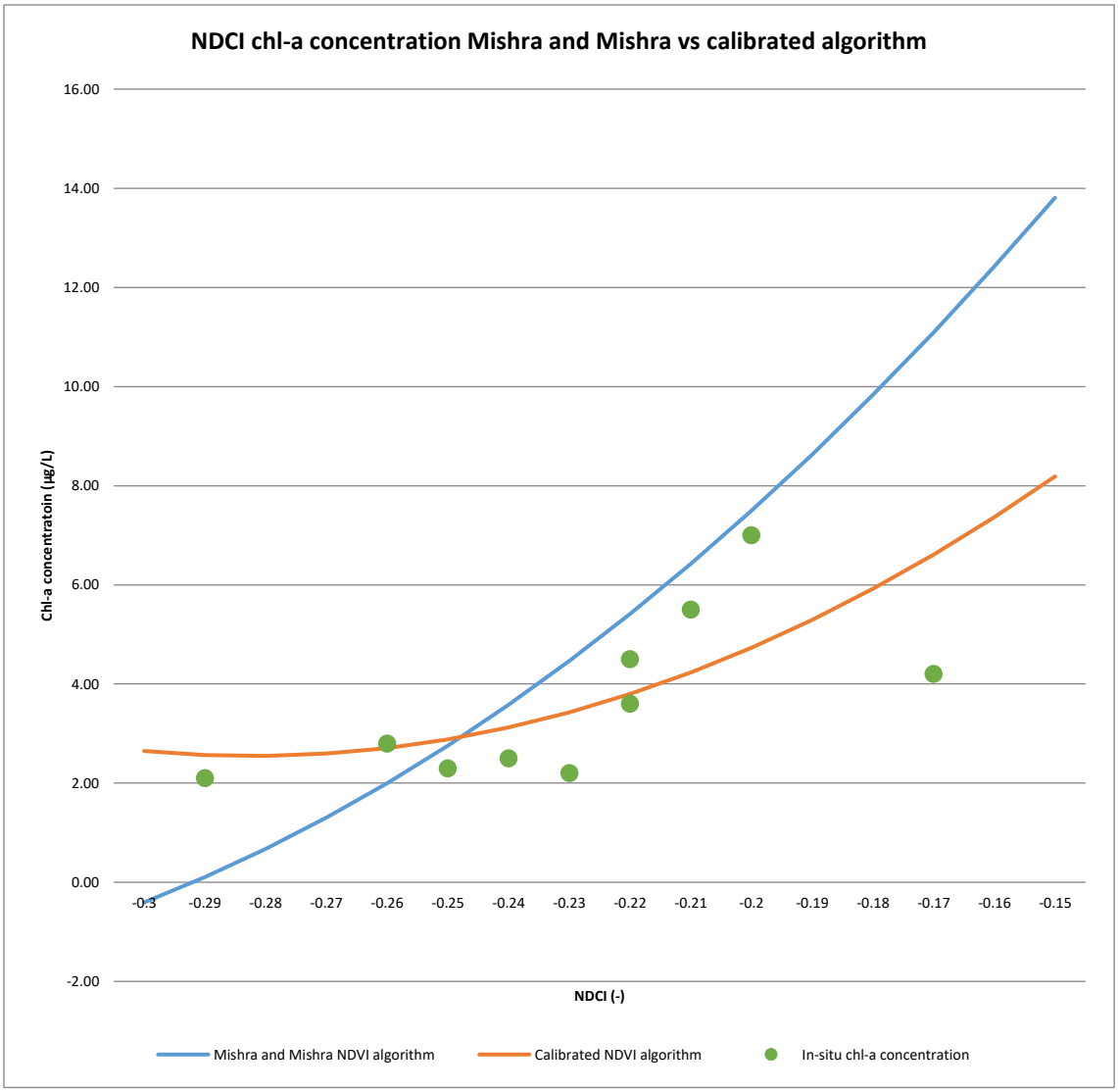

Figure 26 Mishra and Mishra and calibrated NDCI algorithms plotted with in-situ chl-a concentrations, excluding site 12.

	Original	Calibrated	Re-calibrated
MAE	0.94	4.20	2.29
NMAE	0.07	0.23	0.41
RMSE	1.28	9.60	2.48
NRMSE	0.09	0.67	0.55

Table 6 Performance measures for Mishra and Mishra, calibrated, and re-calibrated NDCI algorithms.

3.3. Chlorophyll-a distribution

3.3.1. Gurlin and calibrated band-ratio algorithm

Applying the Gurlin band-ratio algorithm on the whole image resulted in a chl-a distribution map as shown in *Figure 27*. The green colour distribution ranges from 0µg/L to ≥16µg/L, as this distribution showed the clearest distribution with most contrast. Several distribution patterns emerge from this distribution map. The chl-a concentrations were estimated highest in the Danube, upstream of the confluence. The concentration in the Sava were estimated lower, with slightly higher concentrations further upstream. At the confluence (*Figure 28*) there is a clear distinction between the water of the Sava and the Danube, with low chl-a concentration water of the Sava entering the Danube. Notable is that after the first bridge after the confluence, concentrations appear higher. After the confluence, a

cross-river pattern is visible with slightly higher concentrations on the northside, with a gradual decrease towards the other bank. Concentrations prominently exceed the 16µg/L at two locations; at the bay of site 12, calculated at around 110µg/L, and at the lake north of the confluence, ranging from 160µg/L to 200µg/L.

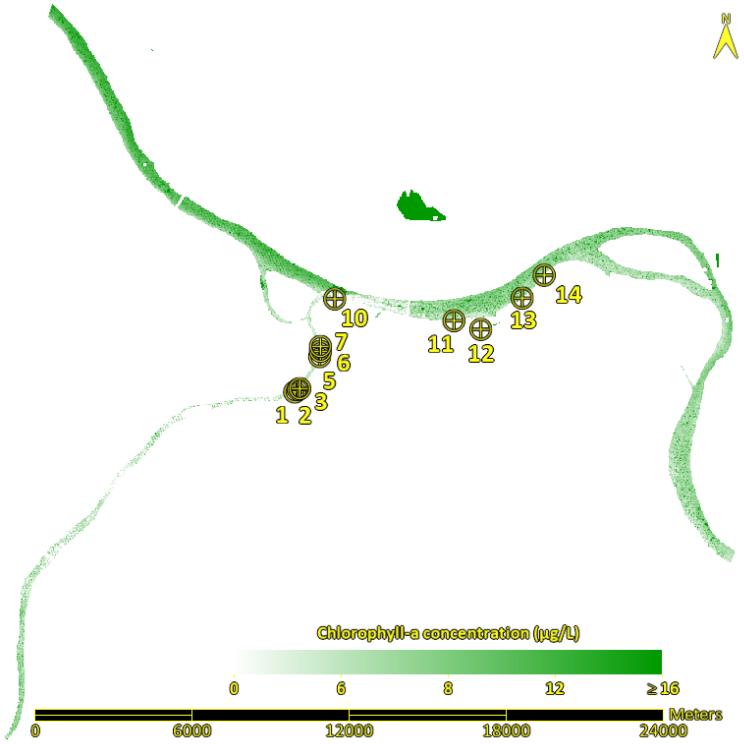

Figure 27 Chl-a distribution of full research area using Gurlin band-ratio algorithm (26-9-2021).

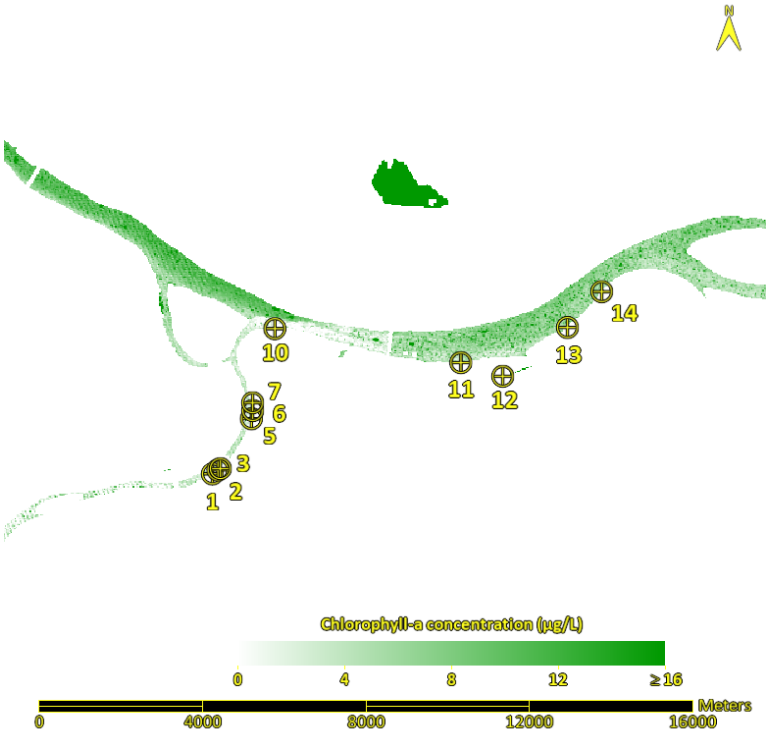

Figure 28 Zoom-in on sampling sites of chl-a distribution using Gurlin band-ratio algorithm (26-9-2021).

Figure 29 is depicted with the chl-a distribution estimated by the calibrated band-ratio algorithm, ranging from 0µg/L to ≥12µg/L. The overall concentrations estimated by this algorithm were lower than those estimated with the Gurlin algorithm. The concentration distribution appears more homogenous, it shows the least spatial patterns of all chl-a concentration distribution maps. The spatial patters at the confluence depicted by the Gurlin algoritm in *Figure 28* do not appear as prominently in *Figure 30*. It only shows a slight decrease in chl-a concentration caused by the Sava joining the Danube.

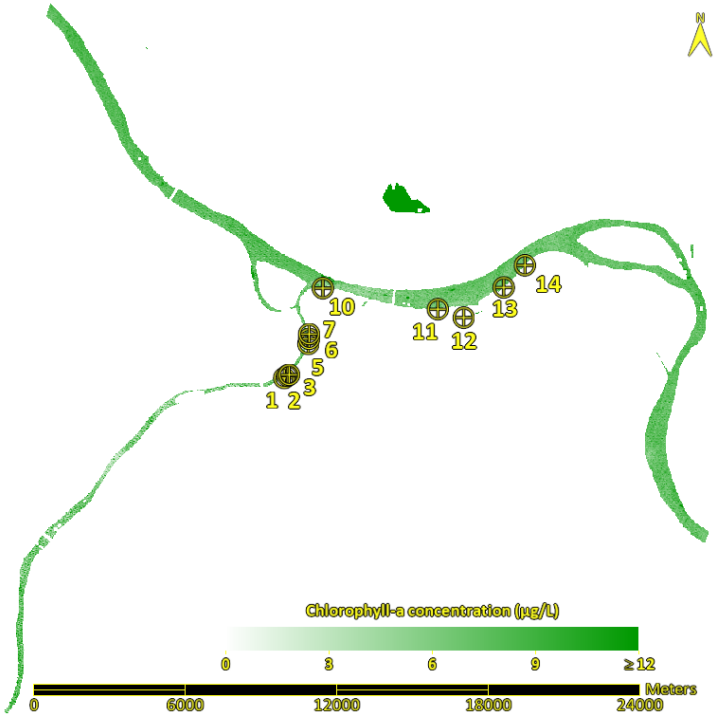

Figure 29 Chl-a concentration of full research area using calibrated band-ratio algorithm (26-9-2021).

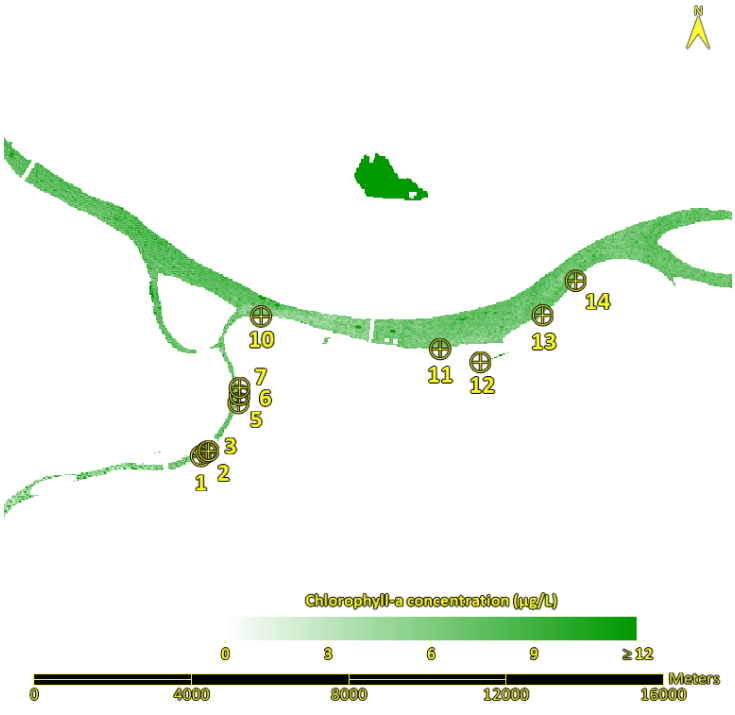

Figure 30 Zoom-in on sampling sites of chl-a distribution using calibrated band-ratio algorithm (26-9-2021).

3.3.2. Mishra and Mishra and calibrated NDCI algorithm

The Mishra and Mishra NDCI algorithm provided the chl-a distribution map shown in *Figure 31* and *32*. The colour distribution ranges from 0µg/L to ≥26µg/L. The spatial distribution that showed in chl-a distribution of the Gurlin algorithm in *Figure 27* and *28* also appear clearly in this distribution map. Concentrations appear higher upstream of the Danube, with a slight gradual decrease from the north bank to the southern bank. Concentrations were estimated lower for the Sava, and slightly higher upstream. Also at the confluence, a clear decrease in overall concentration is visible, but these instantly increase downstream of the bridge. At the prominent bend of the Danube in the east, the northern branch has slightly higher concentrations than the southern branch.

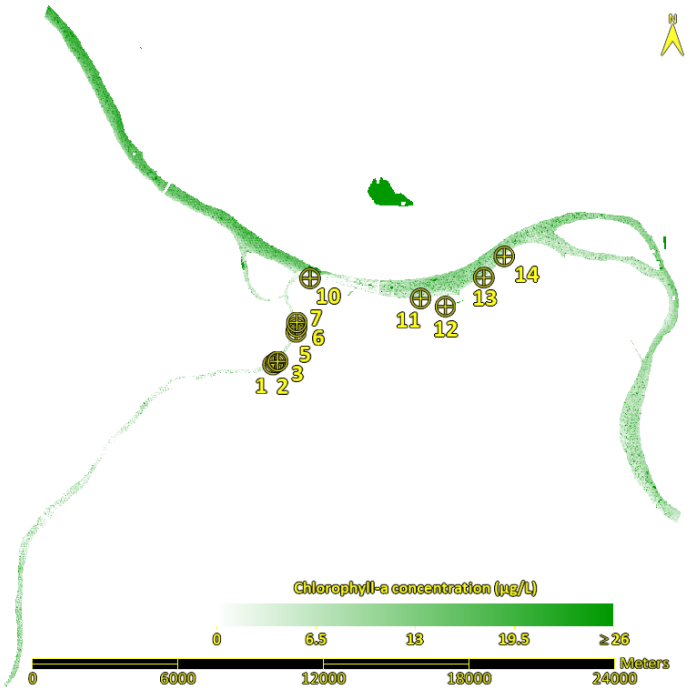

Figure 31 Chl-a distribution of full research area using Mishra and Mishra NDCI algorithm (26-9-2021).

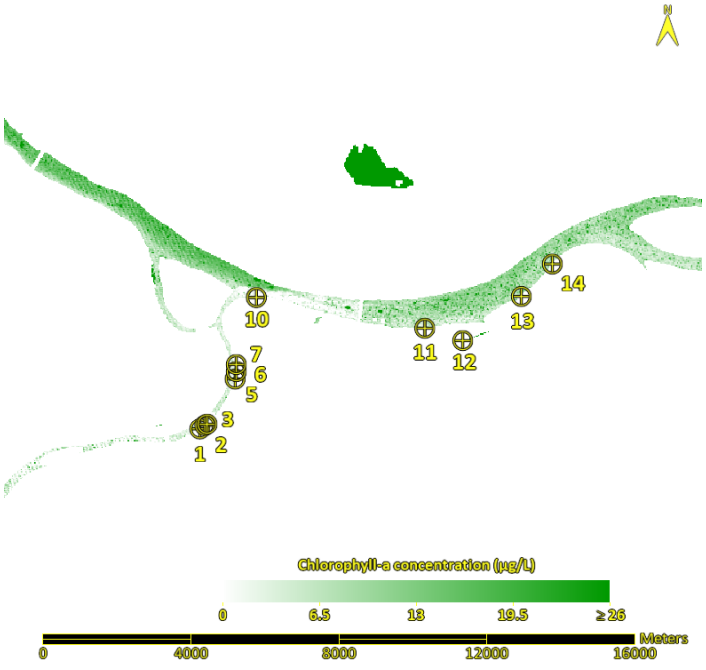

Figure 32 Zoom-in on sampling sites of chl-a distribution using Mishra and Mishra NDCI algorithm (26-9-2021).

The results from the calibrated NDCI algorithm are depicted in *Figure 33* and *34*. Where the calibrated band-ratio algorithm showed little spatial variation in chl-a concentration, this algorithm with similarly poor performance measures, did show the expected spatial patterns. The chl-a concentrations were predicted highest in the Danube, upstream of the confluence. The concentration in the Sava were predicted lower, with slightly higher concentrations further upstream. At the confluence there is a distinction between the water of the Sava and the Danube, as a prominent lower concentration is shown at the confluence. After the first bridge after the confluence, concentrations appear higher. After the confluence, a cross-river pattern is visible with slightly higher concentrations on the northside, with a gradual decrease towards the other bank.

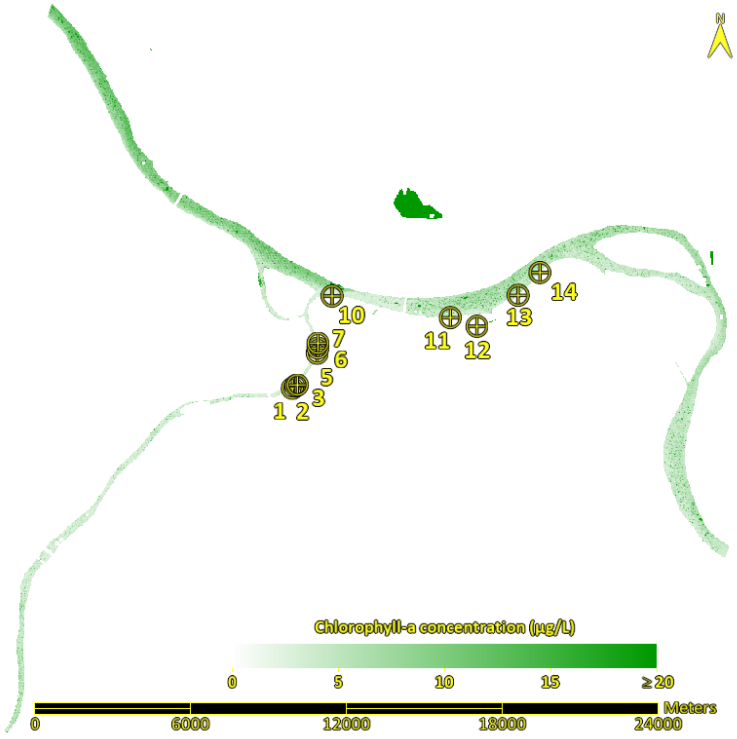

Figure 33 Chl-a distribution of full research area using calibrated NDCI algorithm (26-9-2021).

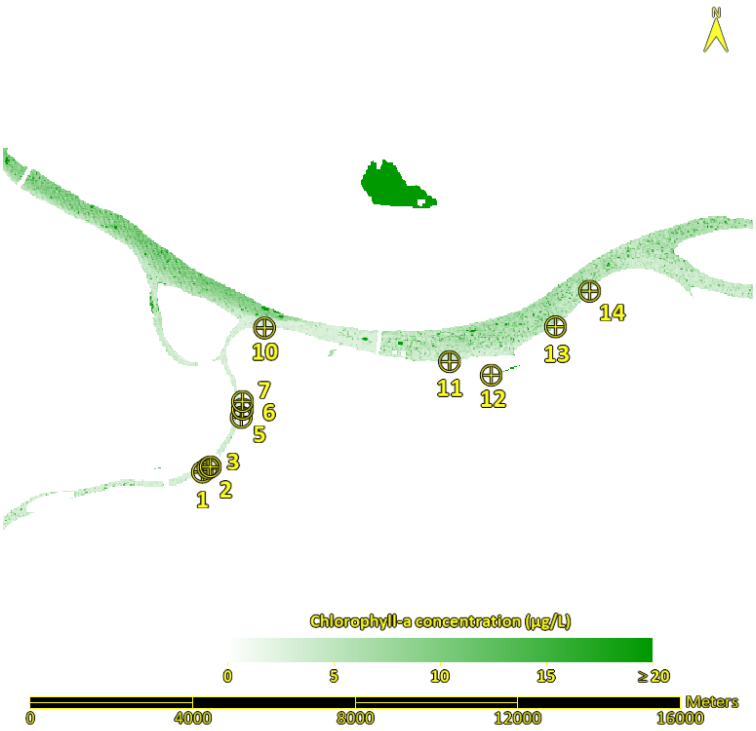

Figure 34 Chl-a distribution at sampling sites using calibrated NDCI algorithm (26-9-2021).

4. Discussion

This study aimed at evaluating how accurate ASI PRISMA hyperspectral images can be used for mapping chl-a patterns in rivers. This *Discussion* section reviews the methods and results of this research, draws conclusions from the results, and proposes topics of future research on this topic. Before the results are discussed, all steps of the methodology are first thoroughly reviewed, covering the sampling process, image preparation, and the calibration and validation methods. After this, the performance of the algorithms is discussed, and the best performing algorithm is selected. This part covers the answering of the first and second research questions of this research on the performance of existing chl- algorithms and the possible improvement after calibration with a local dataset. The results from this algorithm are used to analyse the spatial distribution of chl-a at the Danube-Sava confluence and sources of chl-a are detected, covering the third research question. Research that has covered the methodology and/or topics from this research is discussed next to support the discussion. Next, the analysis is made if the findings in this research would support the development of a chl-a monitoring system, aiming to answer the fourth research question. Finally, propositions are made for future research, as there is still a lot of ground to cover on this topic.

4.1. Review of the methods

4.1.1. In-situ sampling

It proved a difficult process to obtain a timely combination of a hyperspectral satellite image of a river area and multiple in-situ water quality samples taken within a half hour timespan around the satellite image acquisition. Still, it was made possible by thorough planning and a continuous readiness of multiple colleague researchers in Belgrade to take in-situ samples at short notice. The timeframe of a possible image acquisition of PRISMA was known only 9 days in advance, with a confirmation of the actual acquisition 1 to 2 days in advance. Multiple planned image acquisitions failed due to poor weather conditions and high cloud coverage in the study area. All available capacity, both in manpower and equipment, was utilized and the results were very helpful in answering the research questions.

Nevertheless, there are ways to improve in-situ sample acquisition for future research. Firstly, more in-situ samples would enable a more accurate validation of an existing algorithm. Also, the calibration and subsequent validation of a new algorithm would improve in quality with a larger dataset, as this would enable larger separate datasets for calibration and validation. Secondly, a wider spatial variety of the sampling locations would also improve a dataset. This could not take place, again because of the limited capacity to take samples. Samples were taken from the western bank of the Sava, southern bank of the Danube, and in a small bay in the Danube. The Sava has overall lower chl-a concentrations, the concentrations in the Danube downstream of the confluence are lower than upstream, and results from multiple algorithms show that concentrations on the southern bank of the Danube are lower than on the northern bank. With exemption from site 12, the chl-a concentration range of the in-situ samples are homogenous. If samples are taken from the Danube upstream of the confluence and on the other banks, it is likely a more heterogenous dataset is created with higher chl-a concentrations. Finally, a more accurate dataset could be built if samples are taken from locations which would also have pixels usable for analysis in the image. All samples were taken from the bank, with exemption of site 12, which was taken from a jetty. All pixels that were overlapping with the riverbanks had to be removed, and reflectance from multiple usable pixels in proximity was taken instead. If a sample falls within a pixel usable for analysis, reflectance can be extracted from only this pixel instead of a group of pixels. This is also the case for sampling sites that are located in close proximity to bridges, floating barges, ships, or harbour facilities, as was the case for sampling sites 1, 3, 7 and 12. Taking samples from a boat at least 45m, the diagonal of a VNIR PRIMSA pixel, away from the bank or other objects would avoid mixed pixels.

4.1.2. Image preparation

The PRISMA images are made available with a standard georeferencing with an accuracy up to 200m. The exact location of the in-situ samples could not be located using the GPS-grid of the image. They had to be located manually and visually using the 5m spatial resolution panchromatic images and aerial images from Google Earth that did show the correct location of sites. Based on the 30m resolution of the RGB images, it is estimated that the sites were in the imagery with an accuracy of one 30m pixel. It is possible to receive PRISMA images with an accurate georeferencing if Ground Control Points (GCP) are available for the area (Agenzia Spaziale Italiana, 2020). Using such imagery increases the accuracy of the reflectance retrieved from pixels located over sampling sites. For images of the Danube-Sava confluence, no GCPs were available.

In the process of avoiding and removing pixels with mixed values from the analysis, some features were overlooked. In the application of the original band-ratio and NDCI algorithm, as well as the calibrated algorithm, local elevated chl-a concentrations were predicted that were concentrated to 1 to 4 pixels, As can be seen in *Figure 35-38*, these elevations were located where large ships, barges or bridges were present. Removing and masking out these features from the image was not achieved during pre-processing. The reflectance that these features added to the pixels' average were such that the algorithms falsely registered these as a relatively high chl-a concentration. This phenomenon can also be caused by a large number of smaller objects. As depicted in *figure 39* and *40*, a large number of small, recreational vessels are anchored evenly distributed over the southern, left arm in the confluence. These vessels cause a change in reflectance values and hence, an apparent increase in chl-a concentration as well. As these phenomena occurred at only a few locations and as these locations were known, it did not affect the interpretation of the chl-a distribution patterns. The decision was made to not redo the image preparation and remove the mixed pixels in order to estimate the chl-a concentrations without these mixed pixels.

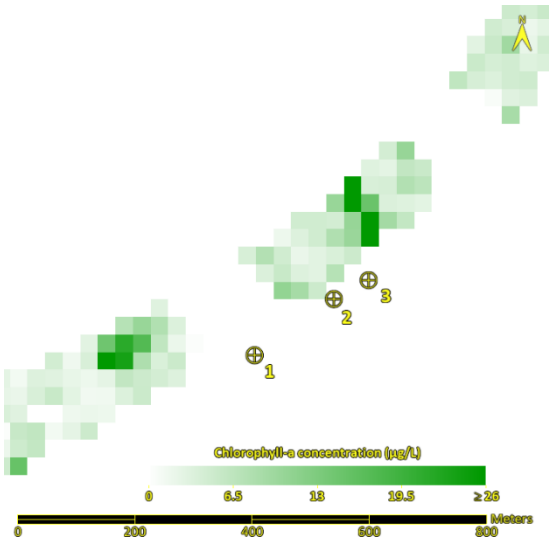

Figure 35 Elevated chl-a concentrations at locations of a ship and bridge in Sava (chl-a distribution Mishra and Mishra NDCI algorithm, 26-9-2021).

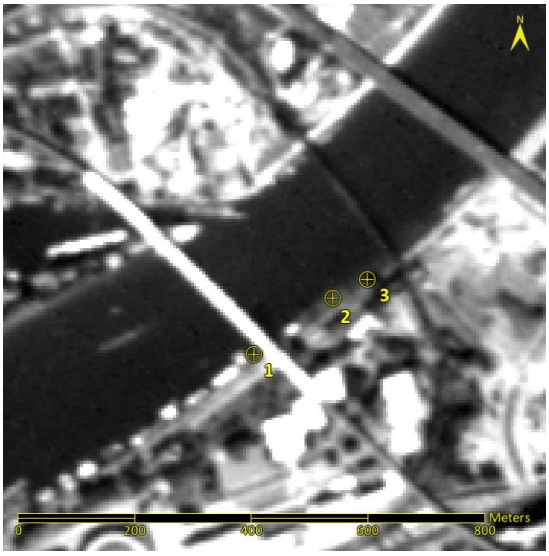

Figure 36 Locations of a ship and bridge in Sava (pan, 26-9-2021).

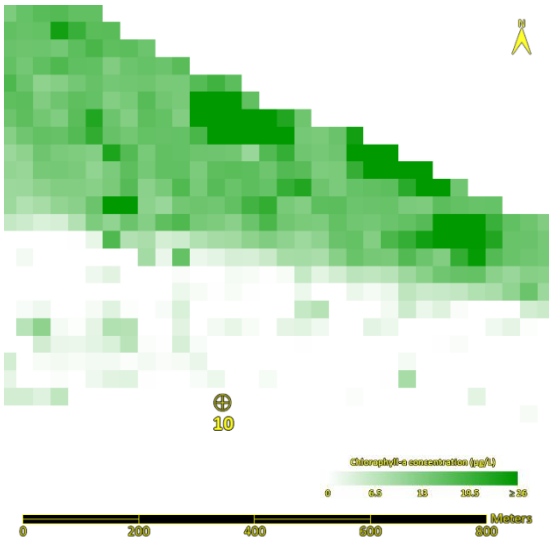

Figure 37 Elevated chl-a concentrations at locations of ships in Danube (chl-a distribution Mishra and Mishra NDCI algorithm, 26-9-2021).

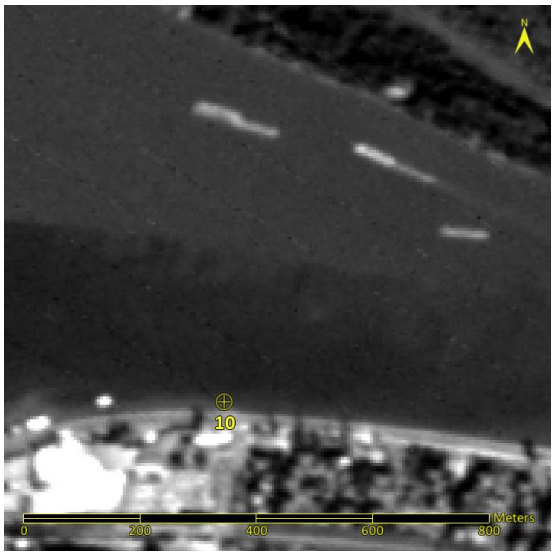

Figure 38 Locations of ships in Danube (pan, 26-9-2021).

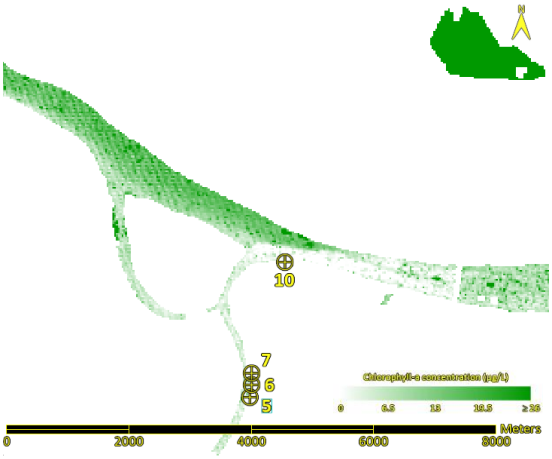

Figure 39 Chl-a distibution at confluence (chl-a distribution Mishra and Mishra NDCI algorithm, 26-9-2021).

Figure 40 Confluence of Danube and Sava (pan, 26-9-2021).

4.1.3. Validation of the original algorithms

A small but well in time with satellite overpass matching dataset comprising of 11 in-situ samples was used to validate the original band-ratio and NDCI algorithms for application on the research area. This dataset is smaller than those used in the USA when developing the models. Gurlin et al. (2011) used two separate datasets for the calibration and validation of their band-ratio model. 89 measurements gathered at the Fremont Lakes Stage Recreation Area in Nebraska, USA in 2008 were used for the calibration of their model. The validation took place with a dataset comprising of 63 measurements from that same area, taken in 2009. The Mishra and Mishra NDCI algorithm was calibrated and validated using both a simulated dataset and a field dataset (Mishra & Mishra, 2012). For the calibration and validation using the field dataset, of the 49 samples, 29 were used for calibration and 20 for validation. The dataset for validation for this research is smaller than those of others, but with 11 samples a validation can still be performed of which the results should be a good initial indication of applicability of chl-a concentration algorithms on rivers.

As discussed, the dataset used in this research is, apart from site 12, homogenous for an area where the chl-a concentrations vary more. Results of several algorithms do show that the chl-a concentration is higher in the Danube upstream of the confluence than at most of the sample locations. The results of the Mishra and Mishra NDCI algorithm show the chl-a concentration ranges from 16µg/L to 20µg/L. Even though the concentrations measured range from 2.1µg/L to 7.0µg/L and do not cover the full range of concentrations present in the research area, it was assumed they would have enough variance for an indicative validation to be performed with.

4.1.4. Calibration of the algorithms

The calibration was performed using a quadratic regression. Another form of regression, like a linear regression, was not chosen because the original algorithms from Gurlin et al. (2011) and Mishra and Mishra (2012) used a quadratic regression in their most successful calibrations. Performing the same regression would offer the best comparison between the original and calibrated algorithms. The band-ratio model was calibrated using a linear regression in Gurlin et al. (2011) as well, but this algorithm had a lower performance.

In Gurlin et al. (2011) and Mishra and Mishra (2012), calibration took place with a dataset comprising of respectively 89 and 29 samples. The full dataset for this research contained only 11 samples and there were no options to extend this dataset for this research. To still work with this limited dataset, the question arose if this dataset was enough for an accurate calibration. 11 samples were not enough to calibrate a model to depict accurate absolute values for chl-a concentrations. It was assumed that 11 would be enough to calibrate a model with the purpose of making estimations of chl-a concentrations. The choice was made to use all data for the calibration of the algorithm, leaving none for a separate validation. With only 11 samples, it was assumed that every sample was needed for the most accurate calibration. Reserving samples for a separate validation would decrease the already limited accuracy.

4.1.5. Validation of the calibrated algorithms

Gurlin et al. (2011) used two datasets for calibration and validation, while Mishra and Mishra (2012) reserved part of one dataset for validation. The choice was made not to do either in this research and the algorithms were calibrated using the full dataset without reserving data for validation. To make a more reliable validation, the algorithms were recalibrated with only 8 samples, reserving 3 for validation. Validating the calibrated algorithms using the same data used for training yielded bias results that did not show an accurate performance of the algorithms. The performance of the calibrated band-ratio algorithm was presented as outstanding after validation, while the recalibration

showed a much poorer performance. Also, the resulting chl-a distribution map of the calibrated band-ratio algorithm did not show the spatial distributions that were expected and visible in the results from the other 3 algorithms.

The recalibration and validation of the algorithms did put the performance in perspective. The resulting performance measures is not the performance of the calibrated algorithms using the full dataset, as samples are missing from the dataset. It does however serve as an indication, and even a minimum value of the performance, as it can be assumed that accuracy and performance of the algorithm increases with a more extensive dataset.

4.2. Algorithm performance

4.2.1. Performance of the Gurlin and calibrated band-ratio algorithm

Overall, the Gurlin band-ratio algorithm performed moderately, with a NMAE of 0.15 and a NRMSE of 0.24 (*Table 7*). The deviations would still be too high to assume that resulting absolute values for chl-a concentration are highly accurate. The algorithm would serve as a good qualitative indication of chl-a concentration, or as a quantitative estimation where such margin of error is acceptable. This is also supported by the resulting chl-a concentration distribution maps (*Figure 27* and *26*). These maps show a proportional spatial variation of chl-a concentration in spatial patterns that is expected from this area. There is a clear difference in concentration between the upstream part of the Danube, which has a higher concentration, and the Sava with a lower concentration. After the confluence, the Danube shows an overall concentration that is higher than that of the Sava, but lower than upstream of the confluence. At the confluence, there are clear patterns of the convulsion visible of the two bodies of water. In the eutrophic bay of site 12, concentrations were calculated at around 110µg/L, the correct order of magnitude compared with the in-situ observation. Overall, the Gurlin band-ratio algorithm would be suitable for making qualitative estimations for chl-a distribution, or quantitative estimations with a substantial margin of error.

The calibrated band-ratio algorithm performed poorly and the calibration was not an improvement on the original band-ratio algorithm. The performance measures of the recalibrated algorithm are not high, with a NMAE of 0.40 and a NRMSE of 0.49 (*Table 7*). These measures partly make that the performance of this algorithm is classified as poor. The resulting chl-a concentration distribution map (*Figure 29* and *30*) was decisive, as this showed a low spatial variation in chl-a concentrations and did not depict spatial patterns that were expected and observed in the results from other algorithms. The Gurlin band-ratio algorithm was calibrated for the use on large surface water bodies with a dataset containing 89 samples. It is expected that the performance of the calibrated algorithm would improve with a larger dataset, but it is unknown if it would allow the use of a calibrated band-ratio algorithm for the calculation of accurate, quantitative chl-a estimations in rivers.

4.2.2. Performance of the Mishra and Mishra and calibrated NDCI algorithm

The Mishra and Mishra NDCI algorithm performed best of all 4 algorithms, both in performance measures as in the resulting chl-a distribution map. This algorithm showed the best performance measures, with an NMAE of 0.07 and a NRMSE of 0.09 (*Table 8*). The NMAE implies that the calculated concentration would, on average, deviate 7% of the observed values. The resulting chlorophyll-a concentration distribution maps (*Figure 31* and *32*) show the spatial distribution that is expected from this area as well. The results from the validation, though be it from a limited dataset, imply that the Mishra and Mishra NDCI algorithm would serve as a good tool for quantitative chl-a concentration estimations in this area with a certain margin of error. Only further research can determine this margin of error.

The calibrated NDCI algorithm showed similar performance measures as the calibrated band-ratio algorithm. The NMAE of the recalibrated algorithm was 0.41 and the NRMSE was 0.55 (*Table 8)*. Where the chl-a concentration distribution map (of the calibrated band-ratio algorithm was inadequate, the map of the calibrated NDCI algorithm (*Figure 33* and *34*) did show promising results, as it showed all the spatial patterns that were observed in the maps of the Gurlin band-ratio and Mishra and Mishra NDCI algorithms. What is notable is that there is less contrast and overall concentrations are lower compared to the Mishra and Mishra NDCI algorithm. This could indicate that the estimated concentrations are not yet in proportion to one another. The calibration of the Mishra and Mishra NDCI algorithm turned out not to be an improvement. Still, the results from this algorithm did show the expected spatial distribution patterns, indicating that there is a bigger chance of improving the NDCI algorithm through calibration with a larger training dataset than there is of improving the band-ratio algorithm.

4.3. Spatial distribution and sources of chlorophyll-a

4.3.1. Spatial distribution of chlorophyll-a

The results show that it is possible to estimate chl-a concentration in the river water, depict the spatial distribution of chl-a, and discover spatial patterns of chl-a using the Gurlin band-ratio algorithm and the Mishra and Mishra NDCI algorithms. Spatial distribution of chl-a can also be depicted with the calibrated NDCI algorithm. It must be considered that the chl-a concentration estimated is the average concentration of chl-a of the water column up to the depth where light cannot penetrate. It was not possible in this study to estimate what this depth was. The spatial distribution patterns that are visible in the results occur in this water column and any vertical chl-a distribution patterns are not directly visible. In addition to the chl-a distribution map of 26-9-2021 (*Figure 41*), chl-a distribution maps were made for the images of 14-9-2020 (*Figure 43)* and 23-2-2021(*Figure 45)*, all using the Mishra and Mishra NDCI algorithm. These maps are shown with a panchromatic image of the same date (*Figure 42, 44 and 46*).

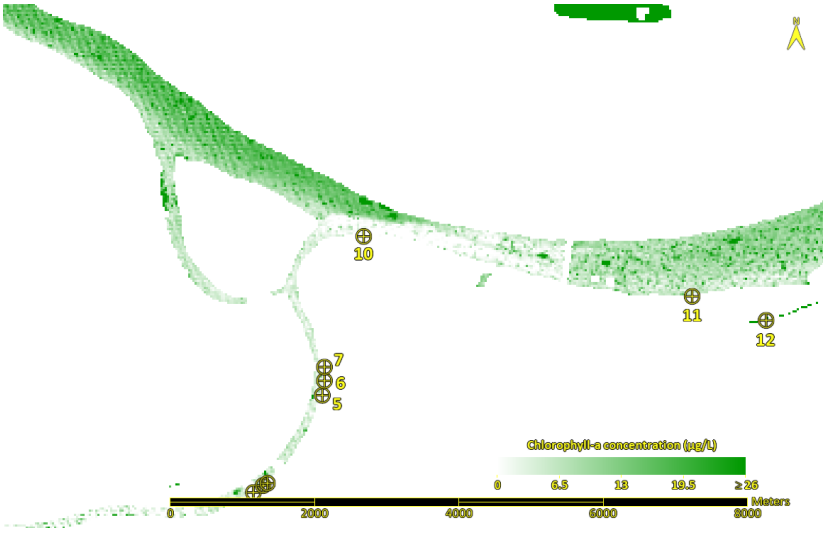

Figure 41 Chl-a distribution at confluence (chl-a distribution Mishra and Mishra NDCI algorithm, 26-9-2021).

Figure 42 Confluence of Danube and Sava (pan, 26-9-2021).

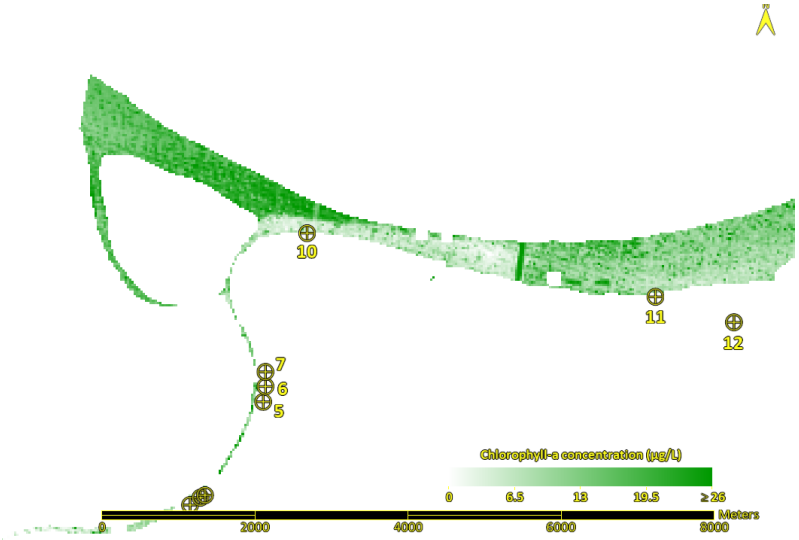

Figure 43 Chl-a distribution at confluence (chl-a distribution Mishra and Mishra NDCI algorithm, 14-9-2020).

Figure 44 Confluence of Danube and Sava (pan, 14-9-2020).

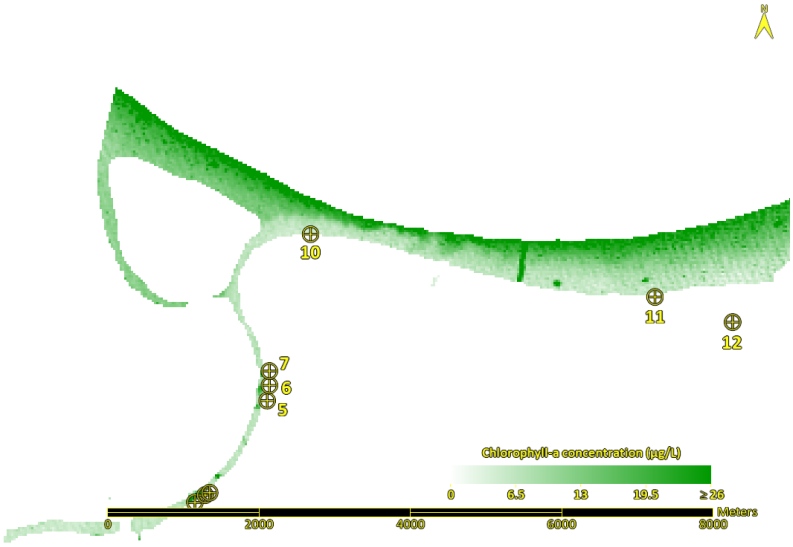

Figure 45 Chl-a distribution at confluence (chl-a distribution Mishra and Mishra NDCI algorithm, 23-2-2021).

Figure 10 Confluence of Danube and Sava (pan, 23-2-2021)

The origins of most large-scale spatial patterns that emerged from these algorithms can be deduced from the chl-a distribution, in-situ data, and knowledge of the area. The mixing of water at and after the confluence is the cause of a prominent spatial patterns. In the panchromatic images, a clear colour difference is visible between the Danube and the Sava (*Figure 42* and 44), the water of the Sava being darker. A clear plume enters the Danube, which can also be seen. The chl-a distribution maps (*Figure 41* and 43) show clear decrease in concentration where the Sava joins the Danube. This lower concentration instantly increases right passing the Pančevo Bridge. A possible explanation for this phenomenon could be due to a difference in water temperature and density in the Danube and the Sava. *Table 9* shows the temperature at the sampling sites, with sites 1 to 7 located in the Sava, site 10 at the confluence, and sites 11, 13 and 14 in the Danube. The water temperature of the Sava is overall higher than the temperature of the Danube after the confluence. The largest difference in water temperature measured, the difference between site 1 and site 14, is 2.0°C. It is also assumed the difference in water temperature of the Danube before the confluence and the Sava is larger than that of the Danube after the confluence and the Sava. The water of the Danube assumably warms after the influx of warmer Sava water. This difference of water temperatures suggests a difference in water

densities between the two rivers. A difference in water densities could cause a vertical stratification at the confluence, where the warmer water of the Sava remains more at the surface and the colder water is forced downward and towards the left bank. The pillars and any underground structures of the bridge could break this stratification and force mixing between the two water columns. This process would explain the sudden decrease change in concentration after the bridge and seems most likely, as it is supported by the measurements of the water temperature at the sampling sites.

Sampling site	Temperature (°C)
1	21.2
2	21.1
3	19.8
5	20.7
6	21
7	21.7
10	20
11	19.2
12	21.9
13	19.5
14	19.2

Table 7 Water temperature at sampling sites.

This phenomenon is not visible in the imagery of 23-2-2021. The panchromatic image (*Figure 46*) does show a cross river colour difference, with water on the northern bank, originating from the Danube, is lighter. The chl-a distribution map (*Figure 45*) shows a chl-a concentration difference between the Danube and Sava. Mixing appears limited and a cross-section difference in chl-a concentration remains. The instant mixing of water after passing the Pančevo Bridge did not occur. This might be due to a less prominent difference in water temperature. This image was acquired in winter, while both other images were acquired at the start of autumn.

After the Pančevo Bridge, there remain a cross-river gradient in chl-a concentration (*Figure 31*), with higher concentrations on the northside bank and lower concentrations towards the southside bank. This could be due to the waters of the two rivers not being fully mixed, with higher concentration water of the Danube remaining on the northside of the river, and water of the Sava remaining on the southside.

The bay in site 12 has a very high chl-a concentration compared to the rest of the research area (*Figure 41*). This bay has stagnant water, and a wastewater outlet resides at the inland end of the bay (*Figure 6*). This makes for a local eutrophic environment that was detected by the algorithms. *Figures 43* and *45* do not show values for this bay. The image preparation process was not able to distinct the full area of this bay, causing remaining pixels to be left out after creating a buffer zone to remove mixed pixels.

4.3.2. Deduction of sources of chlorophyll-a

The large-scale sources of chl-a, like the influx from tributaries, can be deduced from the chl-concentration maps. The initial chl-a concentration in the Danube before the confluence is higher than the concentration in the Sava, as can be deducted from the chl-a distribution map of the full area (*Figure 31)*. The overall chl-a concentration in the Danube decreases after the confluence, which can be attributed to the confluence with the lower concentration water of the Sava entering the Danube.

Where large scale sources and changes of chl-a can be deduced, small scale sources of chl-a were more difficult to observed. The magnitude of changes in local chl-a concentration caused by such sources appeared to be similar to the overall spatial variation in chl-a concentration. Several outlets of untreated wastewater are located within the research area. In-situ measurements performed upstream and downstream such outlets showed a clear change in water quality. Sites 1 and 2, and 5 and 6 are positions upstream and downstream of two outlets. *Figure 6* shows a clear colour difference in the water at the outlets. At the outlet between sites 1 and 2, sampling showed an increase in chl-a, from 2.3 µg/L at site 1 to 5.5µg/L at site 2 (*Table 5*). Besides the chl-a, also the TSS and turbidity both increased tremendously, by 750% and 610% respectively. Sampling at the second outlet between sites 5 and 6 only showed a small increase in chl-a, from 2.5µg/L at site 5 to 2.8µg/L at site 6. The TSS and turbidity increased by 110% and 122% respectively. *Figure 35* shows the chl-a concentration at site 1 to 3. Between site 1 and 2, one pixel shows a slightly elevated chl-a concentration. Such elevations do not stand out, as they are limited to one pixel and the concentration increase is only slight. At site 5 and 6, the chl-a distribution map (*Figure 47*) does not show an increase in chl-a concentration that could be attributed to a wastewater outlet either. It can be concluded that it was not possible to distinguish small sources of chl-a using these methods.

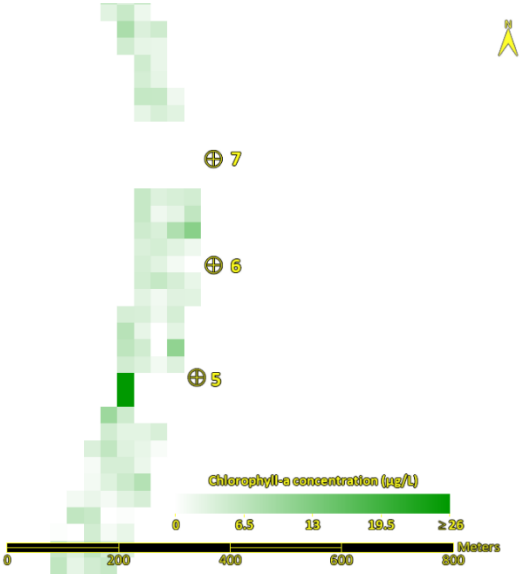

Figure 47 Chl-a distribution at sites 5-7 (chl-a distribution Mishra and Mishra NDCI algorithm, 26-9-2021).

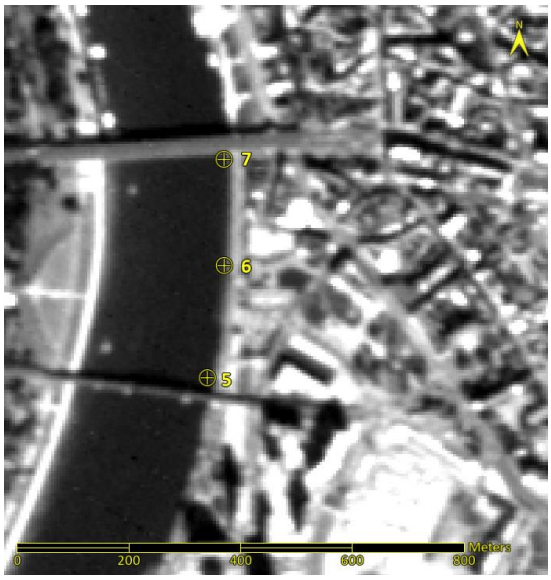

Figure 48 Sites 5-7 (pan, 26-9-2021).

4.4. Supporting research

As mentioned before, only little research has been performed on estimating water quality parameters of river water using hyperspectral satellite remote sensing. Research that covers river water quality analysis through remote sensing is discussed in this chapter. Prasad et al. (2020) developed mathematical regression and artificial neural network (ANN) models to estimate chl-a concentration in the Upper Ganga river. His research is discussed first. Other research studied chl-a in the estuaries of rivers, one of which is Liu et al. (2010), who estimated chl-a concentration sin the Pearl River Estuary from MODIS land bands.

Prasad et al. (2020) used Landsat-8 surface reflectance imagery along in-situ data from a two-year period to develop and validate their models. Reflectance and band-ratios of Landsat-8 bands 2 (450-520nm), 3 (530-590nm), and 4 (640-670nm) were used as input in the form of the band2, band2:band3, band2:band4, band3:band4, band4:band2, and band4:band3. Calibration of each input was done with a linear, exponential, power, and logarithmic function. With 44 samples available for calibration and

18 samples for validation, the composition of these samples was randomly varied to repeat each calibration 20 times, resulting in a total of 480 models. Notable of this approach is the use of band-ratios in the visible part of the spectrum, excluding the NIR part of the spectrum. CDOM has the most prominent absorption in the blue and green part of the spectrum, but also absorbs light in the red and NIR regions (Mishra & Mishra, 2012). Of all these models, the power model of the band4:band2 proofed most successful, with a R^2 of 0.68 and a RMSE of 9.86µg/L after calibration. The validation resulted in a RMSE o 9.5µg/L and a MAE of 7.98µg/L. The results from Prasad et al. (2020) showed that their band-ratio algorithms were comparable to previous research (Duan et al., 2008). The calibration using a logarithmic function yielded the lowest results after validation with a MAE of 53.8µg/L and a RMSE of 54.42µg/L. The fact that a band-ratio of red and NIR reflectance, and a different regression method were used makes it difficult to compare the results of these studies. Prasad et al. (2020) did also construct an ANN model that combines the results from all six reflectance and band-ratio inputs. This ANN can evaluate complicated interactions between variables and present a flexible tool for defining the relationship between remotely sensed images and auxiliary information as input, and biophysical factors as output (Mas & Flores, 2008). It can model a large number of nonlinear relationships without a prior knowledge of the nature of non-linearity (Palani et al., 2008). Prasad et al. (2020) created an ANN model with 20 nodes that produced the best results: a MAE of 1.26 and RMSE of 1.52. This ANN model improved the results produced by the band ratio algorithm. Again, the results of the ANN model cannot be compared with the results of this research as very different methods were utilized.

Liu et al. (2010) aimed to estimate chl-a concentration in the Pearl River Estuary using a band-ratio (band2:band1) of MODIS land bands 2 (842-876nm) and 1 (620-670nmnm). A dataset comprising of 18 in-situ chl-a measurements was created that covered the full extent of the estuary from river mouth to ocean. This dataset is limited in size and comparable to that used in this research. A non-linear relationship between the measured chl-a concentration and the value of the band-ratio. A calibration provided a standard error of 5µg/L and a R^2 of 0.85 for a chl-a range of 5 to 60µg/L. Validation resulted in an average relative error of about 35% and showed that the derived chl-a values fit well with the in-situ measurement in most of the area. This is comparable with the NMAE of the calibrated band-ratio algorithm (0.40) and calibrated NDVI algorithm (0.41). The MODIS bands have a large bandwidth. Band 1 covers the ascend of the absorption peak of chl-a in the red part of the spectrum but does not concentrate on this absorption peak. Liu et al. (2010) concluded that a spectral band more concentrated on this peak would be necessary to predict chl-a concentration more accurately with minimal influence of CDOM. Following this suggestion, PRISMA band 34 at 665nm with a bandwidth below 12nm was used for this research. Liu et al. (2010) concludes that their initial results are very encouraging for the further exploration of chl-a estimation in turbid productive waters using MODIS bands. The model that was applied must undergo further development as the calibration was performed with a seasonally limited in-situ dataset. This model was developed using data from turbid, productive estuarine waters. It would not be applicable to rivers, as the estimated chl-a concentrations turned out high due to the higher concentration of suspended matter in areas close to the river mouth.

4.5. Chlorophyll-a monitoring system

The results of this research show that this methodology could be applied to development of an automated monitoring system that predicts the qualitative chl-a distribution, or values for the absolute chl-a concentration with a certain margin of error. This system could be applied to Danube-Sava confluence and areas similar. With further development, these methods could be developed into a monitoring system predicting accurate, quantitative values with a low margin of error for chl-a concentrations for this area and other rivers. Such a system could be used to observe in temporal changes in chl-a concentration and its distribution patterns, and detect large scale sources of chl-a. It

could also be used to verify results of existing in-situ monitoring systems, replace in-situ monitoring systems, and monitor rivers that beforehand could not be monitored due to lack of accessibility or resources. The rivers it can be applied to are limited to the spatial resolution of the satellite system and the extend that these rivers correspond to the types of rivers including in the calibration dataset.

A river water quality monitoring system must meet certain requirements. The first requirement concerns the dimensions of the river. A river should be deep enough for the bottom not to be visible from above, as this would interfere with the reflectance. The river should also be wide enough for multiple pixels of a satellite system to cover the water surface without overlaying the riverbanks. A wider river would offer the opportunity to better detect spatial patterns and sources of chl-a. The satellite system used must meet certain requirements as well. A high spatial resolution of the sensor used would improve the resolution of the chl-a concentration predictions, better enabling the depiction of spatial patterns. The satellite system must have the spectral bands used in the chl-a algorithm, for this study at 665nm and 709nm, with the appropriate band width, which was ≤12nm for PRISMA. Depending on the requirements of the monitoring system, images of a research area must be acquired with a certain frequency. The satellite system must have an adequate revisit time or the ability to adapt the sensor direction to increase the frequency of image acquiring. Image acquisition is easily affected local weather conditions, which can render images useless for analysis. PRISMA has a revisit time of 29 days, but has the ability to adjust its sensor, enabling image acquisition with a 7-to-10-day interval of the Danube-Sava confluence. Still, it occurred that bad local weather conditions made image acquisition impossible for a 4-week period during the image acquisition for this research. The third important factor is the development of an accurate chl-a concentration algorithm. This development should first entail research to more chl-a concentration algorithms in order to select the most accurate methodology of transforming reflectance values to chl-a concentrations. Algorithms should be calibrated and validated using a more extensive dataset. The dataset should contain data from multiple days, as the water level in rivers and river water constituents vary throughout the year. This dataset should contain data from more sampling sites than it did in this research, as only 11 sites was too few to perform an accurate validation of existing algorithms or calibration and validation of models. If a monitoring system is to be suited for other parts of the Danube or Sava, or other rivers, this dataset should contain data from other areas.

An automated monitoring system should follow the same steps as were followed in this research, with some additions. Firstly, the image acquisition should be automated. This depends on the satellite system that is used, but for PRISMA, this would be possible. When PRISMA imagery is acquired, it is sent over email, so the image would have to be introduced to the system by hand. The system should analyse if the image is usable for analysis, mainly if the cloud coverage is not too high. Through an NDVI, only the area with water can be selected by setting NDVI thresholds that represent pixels with water. An automated land-classification system could also be used. The edges of this selected river area musts be removed to avoid mixed pixels at the banks of the river. Pixels that are mixed due to ships, barges, or small recreational vessels can be removed by better selecting the NDVI threshold, by an automated land-classification system, or by an automated object-based image analysis. After the area to be analysed is identified, the selected algorithm can predict chl-a concentrations for this area. These results can be further analysed by displaying the chl-a distribution mapss, average value of chl-a concentration, and other parameters for the whole research area, or parts of the research area, like certain tributaries or parts of the river.

4.6. Future research

4.6.1. Using different hyperspectral sensors

The research to monitoring water quality through remote sensing has so far concentrated and reported in the literature on large waterbodies, like oceans, lakes, reservoirs, and estuaries. The selection of the research area is limited by the spatial resolution of the satellite system. With the improvement of spatial resolution of hyperspectral satellites, the options for monitoring water quality of rivers can be explored. PRISMA was used for this research, but other satellite or airborne systems could be used if they meet certain requirements: a high spatial resolution, and suitable spectral bands and band widths. Rivers are features that are limited in size compared to lakes or seas. The average width of the Danube near Belgrade is 550m, and of the Sava 300m. A high spatial resolution enables one to remove mixed pixels from large spatial features, like riverbanks and bridges, but keep as much water surface available for analysis and maximizing the data availability. Mixed reflectance of pixels did occur in this research with features that were smaller than the PRISMA 30m spectral resolution, like ships, boats, jetties, and barges, that affected the estimated chl-a concentration. This can also occur with small islands, shallow waters, and even turbulent currents causing scattering. A high spatial resolution, even higher than that of PRISMA, would enable one to identify and remove these features more easily from analysis and avoid mixed pixels. The correct bands and bandwidth are required to retrieve the reflectance of the reflectance peak and absorption peak of chl-a. Lasty, the sensor must have a short return period or the ability to adjust its sensor. Hyperspectral sensor systems meeting these parameters can be used to estimate chl-a concentrations following the same steps as those in this research.

Sentinel-2 suitable for river water quality assessment. This sensor's red band (4) is located at 665nm with a bandwidth of 30nm and a spatial resolution of 10m (European Space Agency, 2015). This is comparable to PRISMA's band 34, with a narrower bandwidth of 10nm, but a higher spatial resolution of 30m. The Sentinel-2 band 5 is located at 705nm with a bandwidth of 15nm and spatial resolution of 20m, comparable to PRISMA band 38 at 709nm. Landsat-8 Optical Land Manager could also be potentially suitable for river water quality assessment. The NIR band covers 850-880nm , which is a higher wavelength than the 709nm band used from the PRISMA sensor (USGS, 2019b). The bandwidth of these Landsat-8 bands is 30nm, wider than the 10nm bandwidth of the PRISMA sensor. Both these factors could possibly affect the results, as other constituents, like CDOM, could start to affect the total reflectance at these bands. MERIS was used by both (Gurlin et al., 2011; Mishra & Mishra, 2012) for water quality assessment, but this sensor is not suitable to research river water. The bands at 665nm (band 7) and 709nm (band 9) with a bandwidth of 10nm (European Space Agency, 2006) are suitable for researching chl-a concentrations. The spatial resolution of 300m renders it not applicable to narrow bodies of water, like rivers.

4.6.2. Different water quality parameters

Not only chl-a could be detected and estimated through remote sensing. Gholizadeh et al. (2016) gathered methods for estimating various water quality parameters of large surface water bodies through remote sensing. These parameters include chl-a, CDOM, Secchi disk depth, turbidity, TSS, water temperature, total phosphorus, dissolved oxygen, biochemical oxygen demand, and chemical oxygen demand. These methods have been developed using a variety of satellite and airborne sensors. These methods were developed for their use on large surface water bodies, not rivers. In this research, two methods for the estimation chl-a concentration were shown to be applicable on river. This does not guarantee that the methods for estimating other water quality parameters can be applied on rivers as the methodology for estimating the other water quality parameters differs from those for chl-a. The shape of a river and other constituents of river water that did not affect the chl-a concentration

estimation can interfere with the estimation of other parameters. Nevertheless, this research showed the possibility for chl-a analysis and should serve as an incentive to investigate the estimation of other water quality in rivers through remote sensing.

4.6.3. Small-scale sources of pollution

Small-scale sources of chl-a, like wastewater outlets could not be localised in this research. Chl-a is a constituent that is not often directly discharged through wastewater. Blooms of algae containing chl-a is not an instant phenomenon, as it is a process that can follow an excessive influx of nutrients (Dodds, 2006). An instant growth of algae shall not occur near an outlet if the water is moved downstream. Other water quality parameters are expected to change more prominently in the vicinity of an outlet. (Polluting) constituents can be directly discharged at a discharge sites. CDOM, TSS and dissolved oxygen could be discharged directly from a discharge site and an increase in concentration is expected near the discharge site. Discharged water can also physiology of local water instantly in other ways. Turbidity and temperature can change locally because of the different turbidity or temperature of the discharged water.

4.6.4. Application on other rivers

The estimation of chl-a concentration as performed in this research can be applied on other rivers as well if the rivers meet certain specifications. A river must be wide enough for the pixels of the satellite system to overlay the body of water; a wider river accommodates more overlaying pixels. To distinguish spatial patterns is then still not guaranteed. With the PRISMA spatial resolution of 30m, it was already hard to distinguish spatial patterns in the Sava, which already has a modest width compared to other European rivers. Rivers should also be deep enough if these methods are to be applied. All methods used in this research assumed rivers were deep enough that the bottom was not visible and did not contribute to the overall reflectance. Lastly, a dataset should be available with in-situ water quality parameters gathered around the moment of capture of the image, that can be used for validation of the existing algorithm used, or for calibrating and validating a new algorithm.

5. Conclusion

Medium resolution hyperspectral imagery is suitable for estimating and monitoring the water quality of rivers. This study shows it is possible to map spatial patterns of chl-a in rivers with qualitative concentration estimates and to refine that into quantitative estimates with a certain uncertainty range. Absolute chl-a concentration mapping remains challenging. Mapping chl-a in surface water is important as it is an important water quality measure and indicative for eutrophication. The Gurlin band-ratio algorithm performed moderately, with performance a NMAE of 0.15 and a NRMSE of 0.24. The resulting chl-a concentration distribution map shows clear patterns as expected from the area. The validation with the limited dataset indicates that the algorithm is suitable for qualitative estimations of chl-a concentrations in the Danube-Sava confluence, or quantitative with a larger margin for error. The Mishra and Mishra NDCI algorithm had the overall best performance, with a NMAE of 0.07 and a NRMSE of 0.09. The chl-a concentration distribution map showed spatial distribution patterns as were hypothesised. Out of all 4 algorithms, this algorithm is best suitable for quantitative estimations of chl-a concentrations in the Danube-Sava confluence with a certain margin of error.

The algorithms did not improve when calibrated with a local training data, probably due to the limited dataset. The calibrated band-ratio algorithm showed the lowest performance and is not usable for qualitative of quantitative estimations. The NMAE of the re-calibrated band-ratio algorithm was 0.40 and NRMSE was 0.49. The chl-a concentration distribution map showed little to none of the spatial distribution patterns that were hypothesised and that were visible in the results of the other 3 algorithms. The performance measures of the calibrated NDCI algorithm were comparable to the calibrated band-ratio algorithm, with an NMAE of 0.41 and a NRMSE of 0.55. The chl-concentration distribution map of this algorithm did show spatial patterns that showed in the original algorithms, including concentration differences between the Danube and Sava before the confluence and (limited) mixing at the confluence. This algorithm should not be applied for qualitative estimations of chl-a distribution, but its original counterpart shows a better performance. Of the two algorithms, the NDCI algorithm has the most potential to improve after calibration with a more extensive local dataset.

The original band-ratio and NDCI algorithms, and the calibrated NDCI algorithm showed clear spatial patterns in chl-a distribution. Large sources of chl-a in rivers, like large tributaries, could be deduced from these distribution maps. These showed that the Danube has the highest chl-a concentration, which decreased after the confluence with the Sava. Small scale sources of chl-a could not be deduced in this research, as the concentration differences at wastewater outlets were not high enough, and the spatial resolution of PRISMA was still too low. If these methods were to be applied on other water quality parameters, possibly with higher resolution sensors, it is likely that small-scale sources of other constituents can be located through remote sensing.

It would be possible to establish a qualitative and quantitative, remote river water quality monitoring system. The Mishra and Mishra NDCI algorithm would be most suitable to be used for this purpose, but it would need to be further validated for its use on the Danube-Sava confluence, or other rivers that this monitoring system would be used for. For the monitoring of chl-a, all steps taken in this research should be automated. Other water quality parameters of larger water bodies, like seas and lakes, can be estimated through remote sensing, and with further research their application of rivers can be made possible as well.

References

Agenzia Spaziale Italiana (2020). *PRISMA Product Specification Document*. Retrieved October 3, 2021, from http://prisma.asi.it/missionselect/docs/PRISMA%20Product%20Specifications_Is2_3.pdf

Agenzia Speciale Italiana (2021). *PRISMA Data Access Description*. Retrieved October 2, 2021, from http://prisma-i.it/index.php/en/data-access/89-data-access/115-prisma-data-access-description

Bhateria, R., & Jain, D. (2016). Water quality assessment of lake water: a review. *Sustainable Water Resources Management*, *2*(2), 161–173. https://doi.org/10.1007/s40899-015-0014-7

Dekker, A. G. (1993). Detection of optical water quality parameters for eutrophic waters by high resolution remote sensing. Free Universit.

Dodds, W. K. (2006). Eutrophication and trophic state in rivers and streams. *Limnology and Oceanography*, *51*, 671–680.

Drazic, D. M., Veselinovic, M. M., Rakonjac, L. B., Bojovic, S. R., Brasanac-Bosanac, L. B., Cule, N. M., & Mitrovic, S. Z. (2014). Geographic, landscape and other natural characteristics of Belgrade as the basis for development of tourism. In *European Journal of Geography, 5*. Retrieved October 8, 2021, from http://www.forest.org.rs/http://www.forest.org.rs/mvcetiri@ikomline.nethttp://www.forest.org.rs/http://www.ibiss.bg.ac.rs/http://www.forest.org.rs/http://www.forest.org.rs/http://www.forest.org.rs/

Duan, H., Zhang, Y., Zhang, B., Song, K., Wang, Z., Liu, D., & Li, F. (2008). Estimation of chlorophyll-a concentration and trophic states for inland lakes in Northeast China from Landsat TM data and field spectral measurements. *International Journal of Remote Sensing*, *29*(3), 767–786. https://doi.org/10.1080/01431160701355249

Environmental Protection Agency (2020). *Water quality - Belgrade*. Retrieved October 13, 2021, from http://www.sepa.gov.rs/index.php?menu=505000004&id=8020&akcija=showExternal

European Parliament (2000). *Directive 2000/60/EC. Establishing a framework for Community action in the field of water policy*. Retrieved November 27, 2021, from https://eur-lex.europa.eu/eli/dir/2000/60/oj

European Space Agency (2006). *MERIS Product Handbook*. Retrieved December 3, 2021, from https://earth.esa.int/eogateway/documents/20142/37627/MERIS-product-handbook.pdf

European Space Agency (2015). *SENTINEL-2 User Handbook*. Accessed on December 6, 2021, from https://sentinel.esa.int/documents/247904/685211/Sentinel-2_User_Handbook

Gholizadeh, M. H., Melesse, A. M., & Reddi, L. (2016). A comprehensive review on water quality parameters estimation using remote sensing techniques. In *Sensors (Switzerland)*, *16*(8). https://doi.org/10.3390/s16081298

Gilvaer, D. J., Greenwood, M. T., Thoms, M. C., & Wood, P. J. (2016). *River Science research and management for the 21st century*, *1*.

Gitelson, A. (1992). The peak near 700 nm on radiance spectra of algae and water: relationships of its magnitude and position with chlorophyll concentration. *International Journal of Remote Sensing, 13(17), 3367-3373*.

Google Earth (n.d.). Locations of sampling sites 1-14. Retrieved on December 6, 2021, from https://earth.google.com/web/search/belgrade/@44.8154524,20.46867769,129.48386637a,19382.8960411d,35y,-0h,0t,0r/data=CigiJgokCVwICg07_zNAEVkICg07_zPAGdgBXLcb3DhAIVbh4oCwIVPA

Google Maps (n.d.). Map of research area. Retrieved on December 6, 2021, from https://www.google.nl/maps/@44.8287955,20.4533449,14.63z

Gurlin, D., Gitelson, A. A., & Moses, W. J. (2011). Remote estimation of chl-a concentration in turbid productive waters - Return to a simple two-band NIR-red model? *Remote Sensing of Environment*, *115*(12), 3479–3490. https://doi.org/10.1016/j.rse.2011.08.011

ITC. (n.d.). *PRISMA*. Retrieved November 26, 2021, from https://webapps.itc.utwente.nl/sensor/getsat.aspx?name=prisma

Janssen, P. H. M., & Heuberger, P. S. C. (1995). Calibration of process-oriented models. In *Ecological Modelling*, 8.

Kuhn, C., de Matos Valerio, A., Ward, N., Loken, L., Sawakuchi, H. O., Kampel, M., Richey, J., Stadler, P., Crawford, J., Striegl, R., Vermote, E., Pahlevan, N., & Butman, D. (2019). Performance of Landsat-8 and Sentinel-2 surface reflectance products for river remote sensing retrievals of chlorophyll-a and turbidity. *Remote Sensing of Environment*, *224*, 104–118. https://doi.org/10.1016/j.rse.2019.01.023

Liu, D., Chen, C., Gong, J., & Fu, D. (2010). Remote sensing of chlorophyll-a concentrations of the Pearl River estuary from MODIS land bands. *International Journal of Remote Sensing*, *31*(17), 4625–4633. https://doi.org/10.1080/01431161.2010.485212

Mas, J. F., & Flores, J. J. (2008). The application of artificial neural networks to the analysis of remotely sensed data. *International Journal of Remote Sensing*, *29*(3), 617–663. https://doi.org/10.1080/01431160701352154

Menken, K. D., Brezonik, P. L., & Bauer, M. E. (2006). Influence of chlorophyll and colored dissolved organic matter (CDOM) on lake reflectance spectra: Implications for measuring lake properties by remote sensing. *Lake and Reservoir Management*, *22*(3), 179–190. https://doi.org/10.1080/07438140609353895

Mishra, S., & Mishra, D. R. (2012). Normalized difference chlorophyll index: A novel model for remote estimation of chlorophyll-a concentration in turbid productive waters. *Remote Sensing of Environment*, *117*, 394–406. https://doi.org/10.1016/j.rse.2011.10.016

Neil, C., Spyrakos, E., Hunter, P. D., & Tyler, A. N. (2019). A global approach for chlorophyll-a retrieval across optically complex inland waters based on optical water types. *Remote Sensing of Environment*, *229*, 159–178. https://doi.org/10.1016/j.rse.2019.04.027

Olmanson, L. G., Brezonik, P. L., & Bauer, M. E. (2013). Airborne hyperspectral remote sensing to assess spatial distribution of water quality characteristics in large rivers: The Mississippi River and its tributaries in Minnesota. *Remote Sensing of Environment*, *130*, 254–265. https://doi.org/10.1016/j.rse.2012.11.023

Palani, S., Liong, S.-Y., & Tkalich, P. (2008). An ANN application for water quality forecasting. *Marine Pollution Bulletin*, *56*(9), 1586–1597. https://doi.org/10.1016/j.marpolbul.2008.05.021

Prasad, S., Saluja, R., & Garg, J. K. (2020). Assessing the efficacy of Landsat-8 OLI imagery derived models for remotely estimating chlorophyll-a concentration in the Upper Ganga River, India. *International Journal of Remote Sensing*, *41*(7), 2439–2456. https://doi.org/10.1080/01431161.2019.1688888

Rijksoverheid. (n.d.). *Water management in the Netherlands*. Retrieved December 7, 2021, from https://www.government.nl/topics/water-management/water-management-in-the-netherlands

Rijkswaterstaat. (2020). *Protocol monitoring en toestandsbeoordeling oppervlaktewaterlichamen KRW*. Retrieved October 27, 2021, from https://www.helpdeskwater.nl/@211466/protocol-monitoring/

Rijkswaterstaat. (2021). Op naar de volgende stap. *Rijkswaterstaat & Zakelijk En Innovatie*, *7*(2).

Schaeffer, B. A., Schaeffer, K. G., Keith, D., Lunetta, R. S., Conmy, R., & Gould, R. W. (2013). Barriers to adopting satellite remote sensing for water quality management. *International Journal of Remote Sensing*, *34*(21), 7534–7544. https://doi.org/10.1080/01431161.2013.823524

Shafique, N. A., Fulk, F., Autrey, B. C., & Flotemersch, J. (2003). *Hyperspectral Remote Sensing of Water Quality Parameters for Large Rivers in the Ohio River Basin*.

Sutadian, A. D., Muttil, N., Yilmaz, A. G., & Perera, B. J. C. (2016). Development of river water quality indices—a review. *Environmental Monitoring and Assessment*, *188*(1), 1–29. https://doi.org/10.1007/s10661-015-5050-0

Swamee, P. K., & Tyagi, A. (2007). Improved Method for Aggregation of Water Quality Subindices. *Journal of Environmental Engineering*, *133*(2), 220–225. https://doi.org/10.1061/(ASCE)0733-9372(2007)133:2(220)

UNDESA. (2014). *Water for Life Decade 2005-2015*. Retrieved November 10, 2021 from https://www.Un.Org/Waterforlifedecade/Quality.Shtml.

USGS. (2019a). *Landsat 7 (L7) Data Users Handbook*. Retrieved December 2, 2021, from https://prd-wret.s3.us-west-2.amazonaws.com/assets/palladium/production/atoms/files/LSDS-1927_L7_Data_Users_Handbook-v2.pdf

USGS. (2019b). *Landsat 8 (L8) Data Users Handbook*. Retrieved December 2, 2021, from https://prd-wret.s3.us-west-2.amazonaws.com/assets/palladium/production/atoms/files/LSDS-1574_L8_Data_Users_Handbook-v5.0.pdf

Acknowledgement

Throughout the writing of this thesis, I have received a great deal of support and assistance, of which I am grateful.

I would first like to thank Prof. Dr. Steven de Jong and Prof. Dr. Ad de Roo, who as my supervisors supported and motivated me in all phases of this research. Thank you for your all insights on this topic, your patience, for enthusing me to tackle this new subject, and finally for allowing me make use of your vast networks in the water science community. I would like to thank Dr. Michelle van Vliet as well, wo acted as supervisor at the start of this research and as reviewer in the final phase. Thank you for your support and familiarizing me to the world of water quality and statistics.

This research could not have taken place without the contributions of Dr. Stoimir Kolarević and his team at the Institute for Biological Research "Siniša Stanković" of the University of Belgrade. Thank you and your team for gathering the in-situ water quality parameters, and for your patience and flexibility in the process of image acquisition.

Thank you to Wesley de Nooijer for your assistance in setting up the calibration process of the algorithms.

I am grateful for the support of the people close to me throughout this process; my parents and my sister. Finally, I would like to thank my girlfriend Marije. Thank you for your support, encouragement, and your remarkable expertise in planning.